Optofluidics for Microscopy and Sensing

by

Md. Faqrul Alam Chowdhury

B.Sc., Bangladesh University of Engineering and Technology, 2007

A THESIS SUBMITTED IN PARTIAL FULFILLMENT OF
THE REQUIREMENTS FOR THE DEGREE OF

MASTER OF APPLIED SCIENCE

in

The College of Graduate Studies

(Electrical Engineering)

THE UNIVERSITY OF BRITISH COLUMBIA

(Okanagan)

February 2012

Abstract

Optofluidics describes a relatively new area of research that aims to synergistically combine optics and fluidics technologies. In this work, we examine the application and integration of small fluid volumes into two types of optical devices, yielding improvements in either tunability, flexibility, or cost-effectiveness. First, we explore a simple methodology to dispense and shape water droplets for use as the magnifying element in a microscope operating under either reflection-mode or transmission-mode illumination. A water droplet is created at the end of a syringe and then coated with a thin layer of silicone oil to mitigate evaporation. By applying mechanical pressure to the water droplet using a metal tip, the shape of the droplet is tuned to yield focusing properties amenable for microscopy. Images captured using the microscope demonstrate micron-scale resolution, variable magnification, and imaging quality comparable to that obtained by a conventional, laboratory-grade microscope. Next, we develop a surface plasmon resonance (SPR) sensor that exploits the index matching and coating capabilities of fluids. Conventional SPR sensor are implemented using an external light source, optical components to polarize incident light and guide light to and from a metal surface, a coupling device (such as a prism) to convert free-space light into surface plasmons on a metal surface and back into free-space

light, and a light detector. Here, we develop a new SPR device architecture by combining several optical components via index matching fluid, which eliminates the need for a prism and integrates light delivery, light polarization control, surface plasmon coupling onto a thin, flexible substrate. We experimentally characterize the SPR device and find good agreement between experimental reflectivity measurements and a theoretical reflectivity model based on transfer-matrix formalism. By developing these new methods to integrate fluids for both microscopy and optical sensing applications, this work provides results that highlight both the promise and challenges of creating optical systems based on fluids.

Table of Contents

List of Tables

List of Figures

Acknowledgements

This thesis would not have been possible without the help and support of my colleagues, friends, and family.

I am heartily thankful to my supervisor, Dr. Kenneth Chau, for both inspiring and teaching me. He has provided constant encouragement, guidance and support throughout my thesis. He has introduced me to the art of scientific research, the beauty of good experimental design, the value of explaining numerical results not only as mathematical constructs, but also through physical interpretation, the subtlety of clear and accessible scientific writing, the rigors of analytical ability and adherence, and the spirit of intellectual integrity.

I am indebted to many of my colleagues for their support throughout the work and writing, and owe special thanks to Reyad Mehfuz for his assistance in depositing gold layers for the development of a surface plasmon resonance chip. I also give special acknowledgment and thanks to Michael W. Davidson of Molecular Expressions Optical Microscopy Primer for providing permission to use the color plates that accompany second chapter of the thesis.

To my family, who, of all that walk on the earth, are most precious to me, for their support in every endeavor. Also to anyone who finds themselves at a place in life where the question of why seems unanswerable, and to all those who seek and side with the truth.

Chapter 1

Introduction

1.1 Background

Optics are ubiquitous in modern technology. Cameras, disc drives, and microscopes all incorporate optical components, such as lenses and prisms, that enable precise control and manipulation of light. Typically, these optical components are constructed from solid, transparent materials, such as glass or plastic, which are machined with high precision into specific shapes with smooth surfaces. While the construction of optical components from solid materials provides mechanical stability, it does not afford a high degree of flexibility and tunability because the shape of the component is fixed. One approach to increase the adaptability of optical systems is to replace solid optical components with analogous components made from fluids [1–4]. This basic endeavor has given rise to the field of optofluidics, a general term that refers to optical devices that integrate fluidic components [5–8]. There are several advantages to the use of fluids for optical applications - fluids are deformable, transparent fluids such as water are highly abundant and inexpensive, and the surface of a fluid is naturally ultra-smooth due to surface tension [9–13]. The main disadvantage to fluid components, however, is the lack of mechanical stability as compared to their solid counterparts. The

basic challenge in the development of any optofluidic system, therefore, is to design cost-effective infrastructure that maximizes the tunability conferred by the use of fluid, yet mitigates instability.

1.2 Objective

The objective of this work is to introduce, design, build, and test two novel optical systems in which fluids have been used to achieve optical components that would have otherwise been constructed from solids. We first explore an optofluidic microscope in which the objective lens is constructed from a droplet of water attached to the end of a syringe. By varying the shape of the droplet through the application of pressure, the droplet lens achieves tunable focus that can be used for either transmission-mode or reflection-mode imaging with micron-scale resolution. The image quality achieved with the optofluidic microscope is comparable to, but still noticeably less than, the image quality achieved with conventional laboratory-grade microscopes. Nevertheless, the optofluidic microscope developed here boasts the advantages of simplicity, low-cost of implementation, and tunability.

We next explore a surface plasmon resonance (SPR) sensor that exploits index matching fluids [1, 2, 14–16] to enable facile coupling between free-space light and surface plasmons. Conventional surface plasmon resonance sensors typically incorporate a prism coupling element to enable free-space light to channel into surface plasmons. Here, we will demonstrate a surface plasmon resonance sensor design in which the prism is effectively replaced by

a drop of index matching fluid, yielding a configuration that is more compact and cost-effective than the conventional prism configuration. The optofluidic surface plasmon resonance sensor is fibre-addressable and integrates the light delivery and polarization control onto a single flexible substrate.

1.3 Thesis Outline

A basic overview of microscopy is given in Chapter 2, which includes an introduction to the physical theory and principles of microscope image formation, an overview of common aberrations observed in microscope images and their causes, and a review of state-of-the-art condenser and objective lens designs for correcting these aberrations. The discussion in Chapter 2 will provide the reader with an appreciation of the aberrations observed in the microscope images captured by the optofluidic microscope.

Chapter 3 describes a simple, low-cost, and elegant configuration for realizing a tunable microscope system using a water droplet as the objective lens. Starting with a review of contemporary research on fluidic lens microscopy, this chapter demonstrates the application of the droplet lens as an alternative and less-explored approach to realize a fluidic lens. The droplet lens consists of a single droplet of water attached to the end of a micro-liter syringe and possesses large acceptance angles, short focal lengths, and a wide tunability range. The focussing properties of the droplet lens are characterized as a function of the droplet size and modeled as a thick lens using both analytical and ray-tracing methods. We apply the droplet lens as a variable, magnifying component in a microscope and demonstrate

microscopic imaging in both reflection-mode and transmission-mode illumination, yielding micron-scale resolution and image quality comparable to that obtained by a conventional laboratory-grade microscope.

Chapter 4 begins with an introduction to the theory and principles of SPR and reviews state-of-the-art SPR sensor geometries. We then introduce the design philosophy of a SPR sensor that exploits the index-matching capabilities of fluids. The proposed sensor consists of a thin gold film on a multi-layer index-matched flexible substrate, which is then optically attached to input and output optical fibres via a drop of index matching fluid. Due to the interconnection between the optical fibre and the substrate via fluid, light transiting from the fibre to the metal film is always immersed in a dielectric, precluding the need for a discrete coupling element such as a prism. We build and test a prototype device, detailing the extraction of SPR reflectance curves from the sensor. The performance of the sensor is compared with a multi-layer reflectivity model derived from transfer-matrix formalism. Model predictions of the spectral position and magnitude of the SPR reflectance dip as a function of incidence angle are in good agreement with experimental measurements.

The thesis concludes in Chapter 5 with a summary of the key findings in the work.

Chapter 2

Basics of Optical Microscopy

A microscope is an instrument that enables visualization of small objects not observable by the naked human eye. The basic optical components of a microscope include an illuminator (a light source and collector lens), a condenser, objectives lenses, and an eyepiece or camera detector [17]. Different combinations of these components are used based on the intended application and desired magnification. In this chapter, we will introduce the basic components of a light microscope, detail common aberrations observed in microscope images and their causes, and review state-of-the-art condenser and objective lens designs that correct for these aberrations.

2.1 Components of a Light Microscope

2.1.1 Illuminator

Microscope imaging requires a beam of light that is bright, uniform, and constant in amplitude. Common light sources include incandescent filament lamps and arc lamps [18]. High performance light-emitting diodes (LEDs) are becoming more popular due to their stable output, low energy consumption, low heat generation, low cost and long life span. Laser sources

are rarely used due to speckle, caused by interference of light scattered within the illumination field. In conjunction with a light source, a collector lens is commonly used to gather the light emanating from the light source.

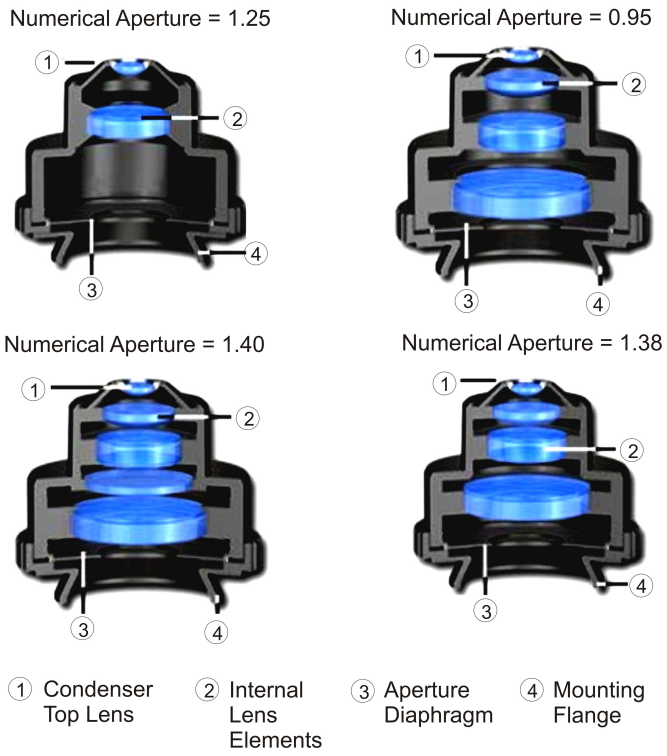

Figure 2.1: Representative image of the internal lens elements inside condensers of different numerical aperture values [19–22].

2.1.2 Condenser

The condenser is an optical element, consisting of multiple lens elements, located between the illuminator and the specimen stage. The role of the condenser is to focus the light from the illuminator onto the imaged region of the specimen. The light cone formed by the beam focussed by the condenser can be adjusted by an adjustable aperture diaphragm.

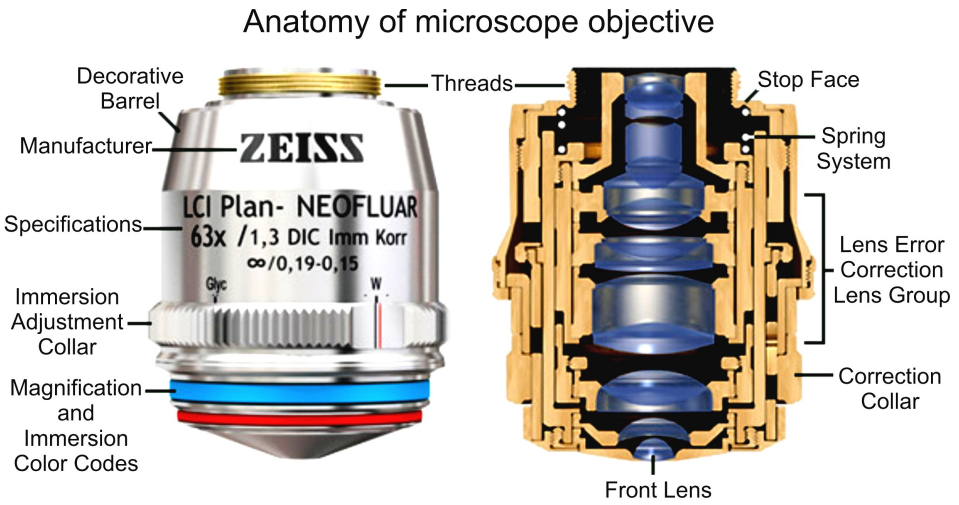

Figure 2.2: Anatomy of a plan-corrected fluorite objective from ZEISS with 63× magnification capability, numerical aperture of 1.3 with oil/water/glycerin as the immersion medium, differential interference contrast (DIC) method, incorporating infinity color corrected system, also having adjustable cover glass correction (Korr) suitable for cover glass thickness range of 0.15-0.19 mm [21, 22]

2.1.3 Objective

The objective is the most critical component of the light microscope. The role of the objective lens is to collect the light from the imaged region of the specimen and to form a real image that is viewed either by a human eye or a camera. In the simplest realization, the objective can be a large magnifying lens with a short focal length. In more complex realizations, the objective can consist of up to fifteen or more lens elements affixed in a permanent housing, as shown in Figure 2.2 [23]. The multiple lens elements in sophisticated objectives are required to correct for imaging errors and aberrations, which will be discussed later in this chapter. Objectives are primarily classified by their numerical aperture and magnification [24]. The

former describes the angle over which the objective can accept light, and the latter describes the enlargement provided by the objective relative to the real imaged region.

2.1.4 Light Microscopy Configurations

The placement of the light source with respect to the other optical components of a microscope depends on the imaging configuration [17, 18, 25]. A microscope intended for light transmission imaging uses the trans-illumination configuration (also known as diascopic illumination), in which the light source and imaging lenses are placed on opposing sides of the specimen. Light emitted from the illumination source is focused onto the specimen by a condenser typically located below the specimen and light transmitted through the specimen is collected by the objective. A condenser aperture diaphragm is a variable aperture placed before the condenser lens. As shown in Figure 2.3, the diaphragm controls the illuminated condenser aperture, enabling adjustment of the angle of the light cone incident onto the specimen. Lighting is optimal when the angle of the light cone matches the numerical aperture of the objective lens on the other side of the specimen.

A microscope intended for light reflection imaging uses the epi-illumination configuration (also known as epi-scopic illumination or vertical illumination), in which the light source and imaging lenses are placed on the same side of the specimen. This type of microscope is commonly used for imaging opaque specimen or for metallurgical investigations. Light from the illumination source is directed onto the objective lens. The objective lens focuses the incident light onto the sample (like a condenser lens in the trans-illumination

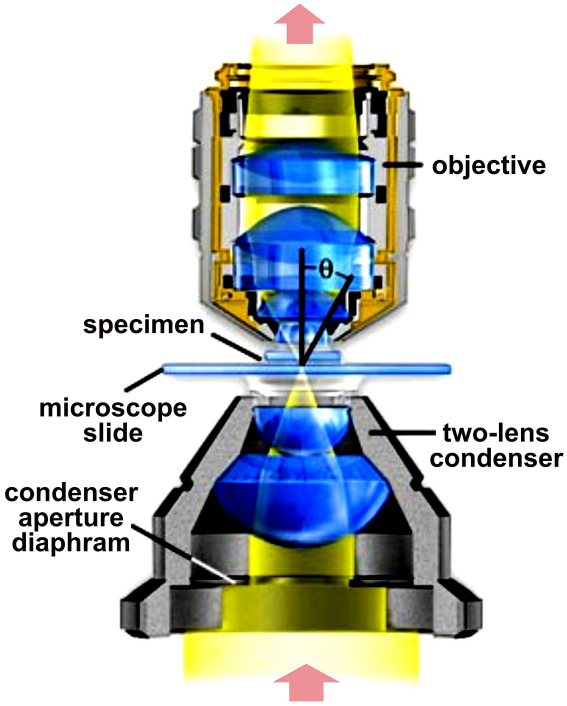

Figure 2.3: Illustration of trans-illumination optical microscopy using a simple objective and condenser, in a configuration known as an Abbe microscope. The aperture controls the aperture of light entering the condenser [19, 20, 22, 26].

configuration) and collects the light reflected from the sample. Compared to trans-illumination, fewer adjustments are required for epi-illumination because the objective lens acts as both the condenser and objective lens. The reflected light collected by the objective lens is then directed onto an imaging device. Because the illumination source and imaging device are on the same side of the specimen, more than one light path is required, which is achieved by using a partially reflecting surface (a dichroic mirror or beamsplitter), as shown in Figure 2.4.

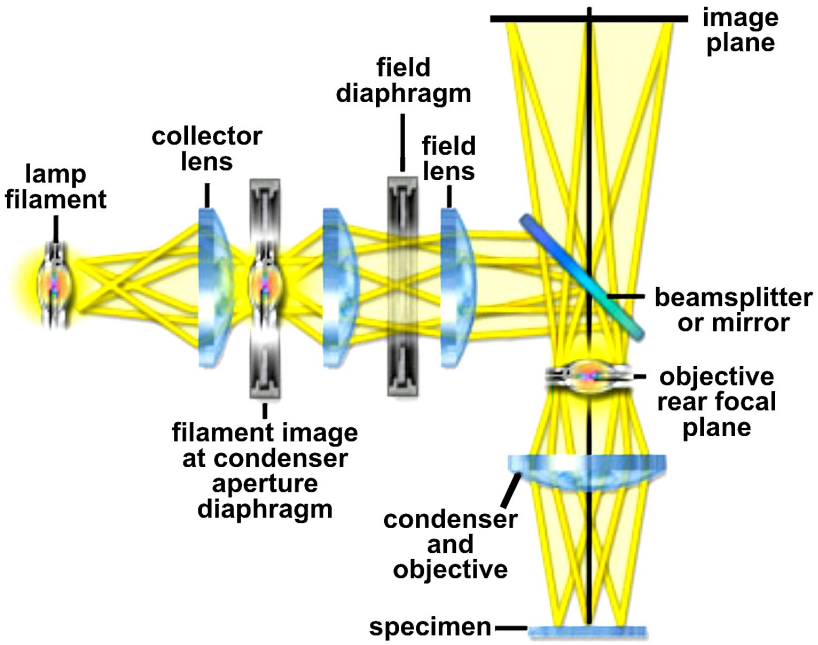

Figure 2.4: Epi-illumination configuration for bright field reflection mode microscopy. Light is directed along the optical axis onto the objective lens. The lens focuses the incoming light onto the specimen, collects the reflected light, and projects the image of the specimen [19, 20, 22].

2.2 Optical Microscopy Concepts

2.2.1 Point Spread Function and Airy Disc

The response of an imaging system is characterized by its point spread function, a term describing the image produced by an optical element due to an ideal point source of radiation. An axially symmetric lens placed near a point source of radiation produces a point spread function that consists of a circular diffraction pattern [25]. Sectioning the diffraction pattern in the transverse plane (perpendicular to the axis of the lens) at the focal point yields the classical two-dimensional diffraction spectrum, which is charac-

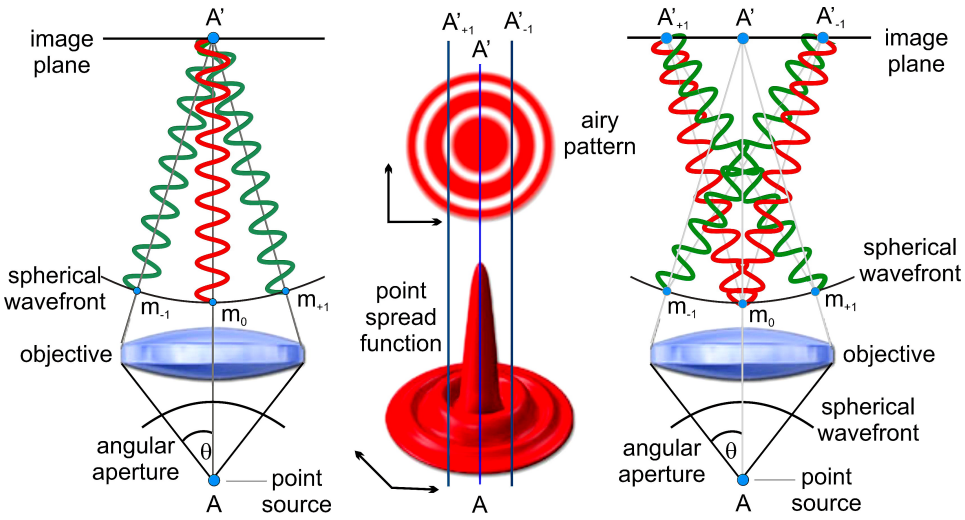

Figure 2.5: Formation of a point spread function (PSF) and resulting Airy pattern. (left) Constructive interference of wavefronts collected by an objective at the point A' results in a bright central region of the Airy pattern and (right) destructive interference at the points A'_{+1} and A'_{-1} results in the dark regions of the Airy pattern [19, 21, 22].

terized by a bright circular disc surrounded by an alternating series of bright and dark rings. This diffraction spectrum is known as the Airy pattern and the central part of this pattern is called the Airy disc. The radius of this inner disc (known as resolution element or resel) provides a measure of the resolving power of an objective. The relationship between the radius of the inner Airy disc and the resolution of an imaging system is shown in Figure 2.6. The series of images on the left panel of the figure depicts two Airy patterns, for various wavelengths, resulting from two point sources representing two closely-spaced features on a specimen. The feature separation in the image is defined by the distance between the centres of the Airy discs. When the Airy discs of the two Airy patterns overlap, it is no longer possible to distinguish the two point sources in the image [26]. The resolution is

then defined as the smallest feature separation that is distinguishable in the image plane as two distinct objects. Note that the resolution of an imaging system tends to decrease as the wavelength decreases [24].

2.2.2 Numerical Aperture

Light gathering capacity of a lens is described by a parameter called the numerical aperture (NA), defined as

$$\mathrm{NA} = n \sin \theta, \tag{2.1}$$

where n is the refractive index of the surrounding medium and θ is the most extreme ray in the light cone. The numerical aperture of a lens can be increased by increasing the lens aperture or by using a high refractive index medium surrounding the lens [17, 24, 26]. The relationship between the numerical aperture of a lens and its resolution is shown in the comparative Airy patterns in Figure 2.6. As the acceptance angle of the objective lens increases, the size of the airy pattern diminishes, meaning that the minimum resolution decreases.

2.2.3 Magnification

The magnification of an imaging system is a dimensionless parameter that describes the relative size of an image of a specimen with respect to its true size. Magnification is a comparatively less important parameter than the numerical aperture. Increasing the magnification of an imaging system past a point where the fine features of a specimen are no longer resolvable

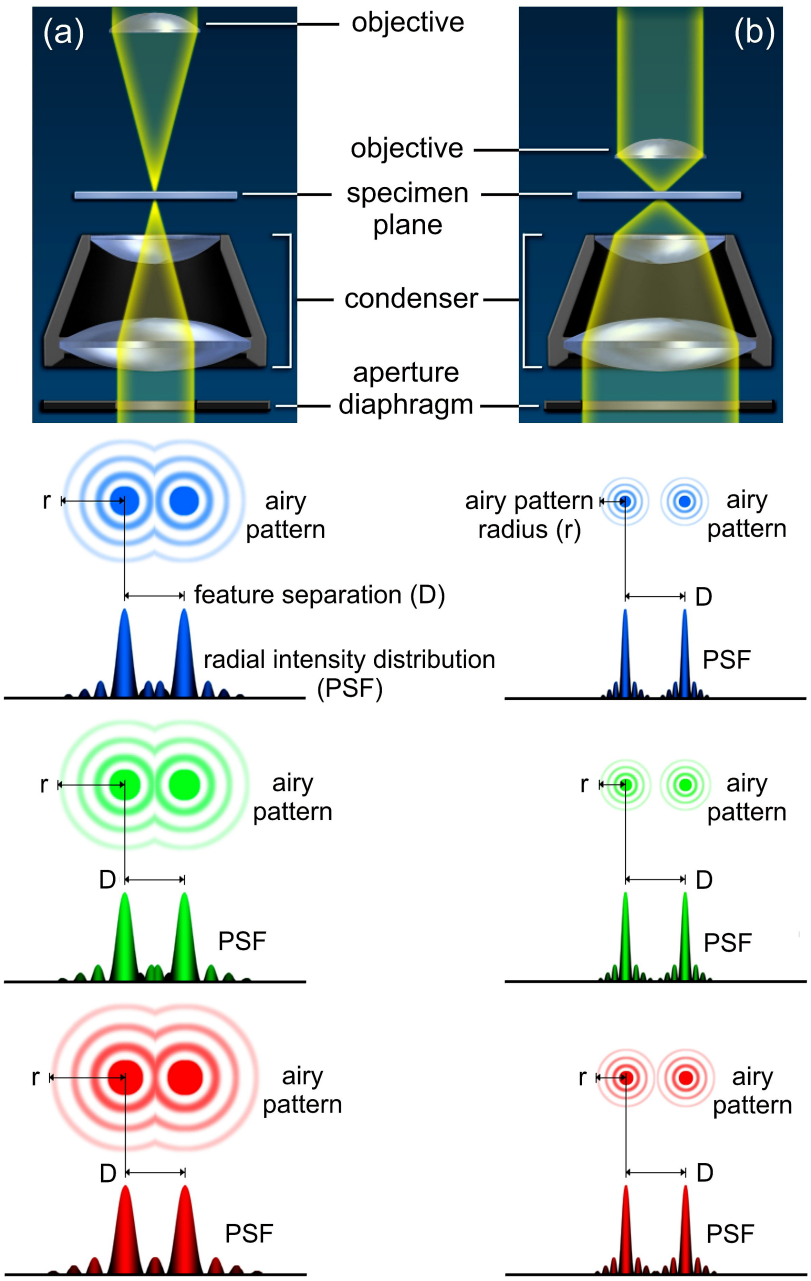

Figure 2.6: Airy pattern resulting from two point sources. The left side illustrates the Airy pattern using an objective with relatively low NA, for three different wavelengths, and the right side illustrates the Airy pattern using an objective with relatively high NA, also for three different wavelengths [19, 21, 22].

does not increase the image detail, but merely enlarges the image with no new information (known as empty magnification) [24].

2.3 Optical Aberrations

Optical aberrations describe faults introduced by an imaging system, and are classified as either (i) chromatic aberrations or (ii) monochromatic aberrations [27]. The former arises from the variations in the refractive index of materials at visible frequencies, and the latter arises from the non-ideal shape of a lens and the deviation of lens performance from first order theory (also known as paraxial or Gaussian optics). Monochromatic aberrations include spherical aberration, astigmatism, and comatic aberration - all of which make an image unclear - and geometrical distortions and Petzval field curvature - both of which deform an image.

2.3.1 Spherical Aberration

Spherical aberrations are the most common resolution artifact and arise when the sphericity of a lens shape causes light rays incident onto different parts of a lens to focus at different points along the optical axis. The cause of spherical aberrations and its effect on the image produced by a lens are shown in Figure 2.7, for the case of three lens with differing degrees of sphericity. Sphericity of the lens shape causes the light rays incident onto different portions of the lens aperture to converge at different points along the optical axis. Due to the different convergence points of the rays, the focal point of the lens is no longer defined at a single point, but rather de-

fined at the point where the diameter of the cone formed by the converging rays is minimum, known as the circle of least confusion, $\sum_{\mathrm{LC}}$ [27]. Increasing sphericity of the lens shape causes the point spread function and Airy pattern to smear out, resulting in a blurring of the resulting image taken at the position of $\sum_{\mathrm{LC}}$. Spherical aberration effects can be reduced by utilizing aspherical lens surfaces, or by limiting the periphery of the lens from exposure to incident rays using aperture-stop diaphragms.

2.3.2 Astigmatism

Astigmatism describes an imaging error where light rays from orthogonal planes have different focal lengths. The point spread function of an imaging system with astigmatism is generally elongated, resulting in an Airy pattern that is elliptical. Because different rays are focussed at different positions, the shape of the Airy pattern changes as a function of distance from the lens. Astigmatism becomes more pronounced for light rays emerging from a point off the optical axis. Figure 2.8 demonstrates the point spread function, Airy pattern, and resulting image of an imaging system that possesses a large degree of astigmatism. For the case of an object point that is well-aligned with the optical axis, the Airy pattern is approximately symmetrical and the resulting image is well-focussed. As the object point moves away from the optical axis, the Airy pattern becomes elliptical and the resulting image become highly dependent on the position of the image plane. Due to the ellipticity of the Airy pattern, either the vertical or horizontal lines of the image are sharp and focussed, but not both.

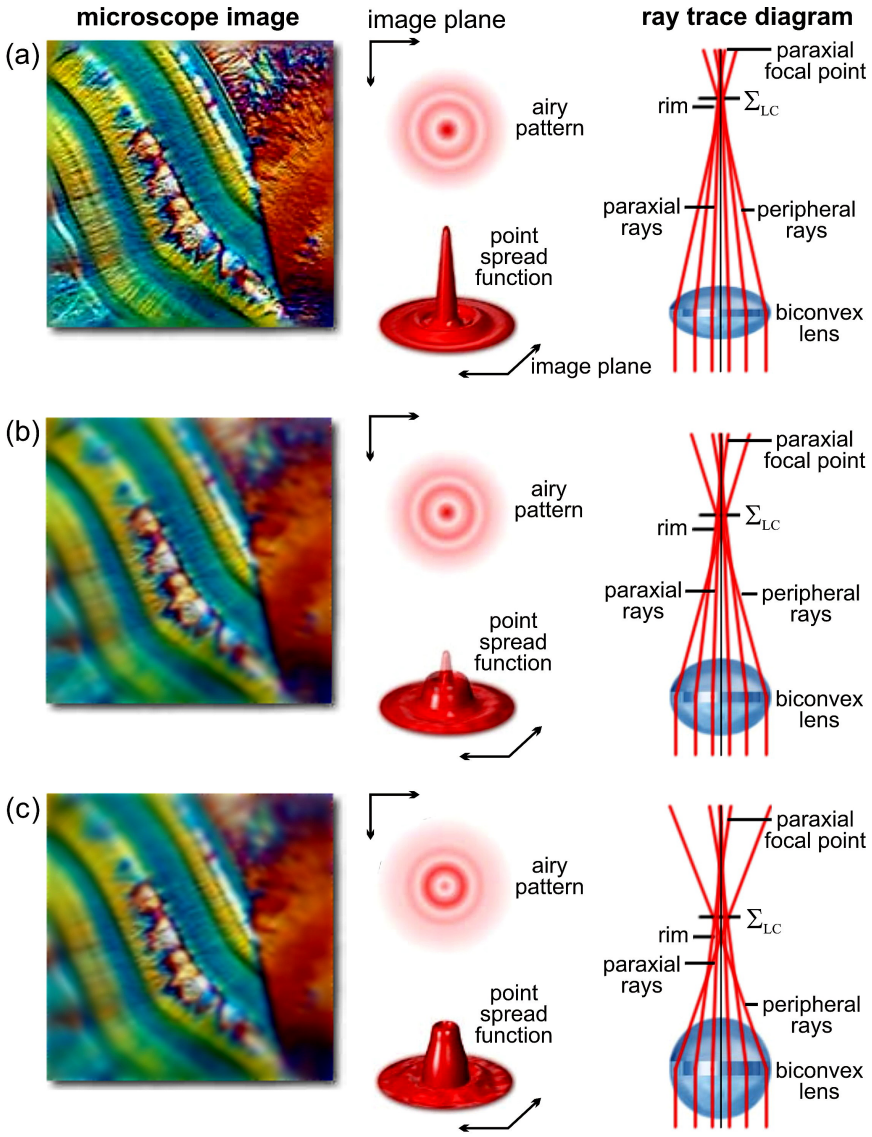

Figure 2.7: The effect of spherical aberration as a function of lens sphericity. The plane of observation is at the circle of least confusion, $\sum_{\mathrm{LC}}$. When the sphericity is less, as in (a), maximum intensity is found at the center of the point spread function, yielding a comparatively clear image. When the lens become more and more spherical as shown in (b) and (c), contrast and detail of the image is degraded even if the image plane is still at $\sum_{\mathrm{LC}}$ [19, 20, 22].

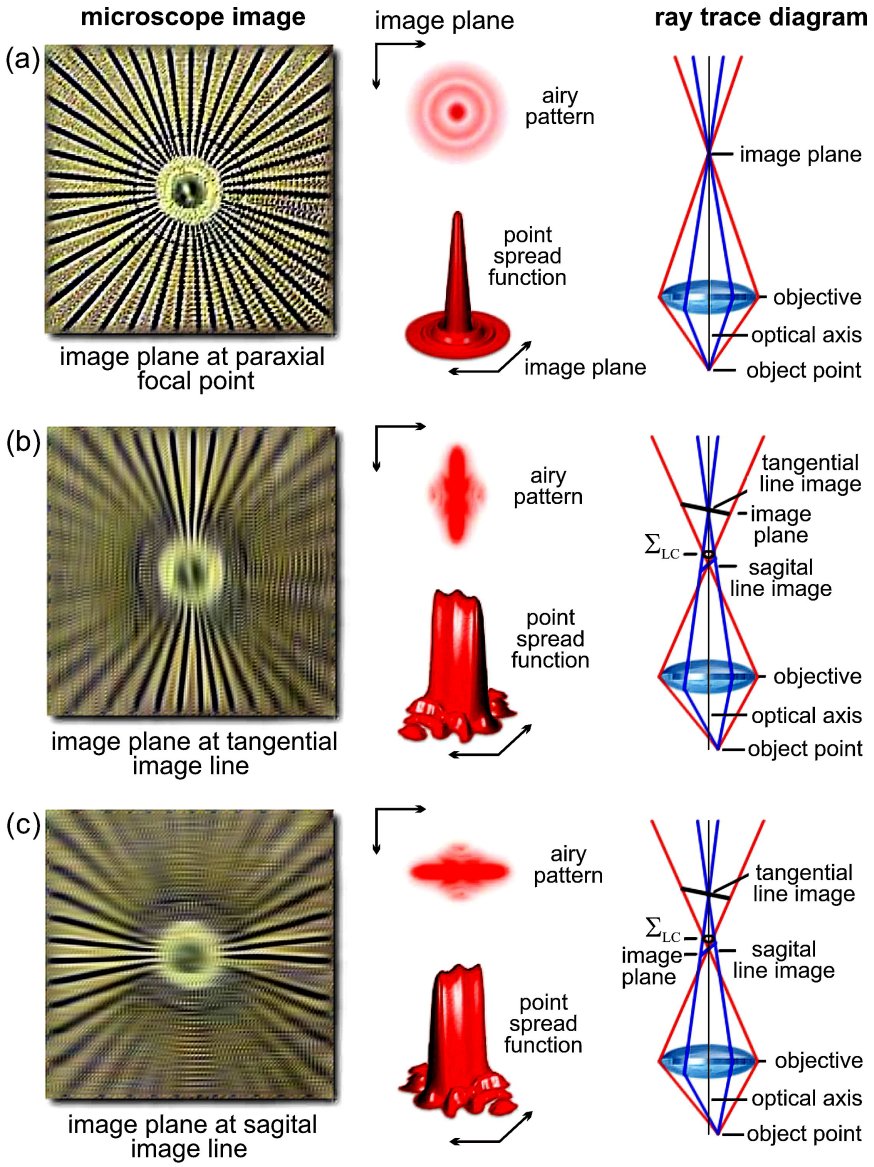

Figure 2.8: Exaggerated representation of the effect of astigmatism on an imaging system for the case of (a) an object point aligned along the optical axis and an image plane located at the focal plane, (b) an object point located off the optical axis and an image plane located at the sagital focal plane, and (c) an object point located off the optical axis and an image plane located at the tangential focal plane. The point spread function, Airy pattern, ray tracing diagram, and resulting image are shown for each case [19, 20, 22].

2.3.3 Comatic Aberration

Comatic aberration or coma is an optical aberration that arises from imperfections in the lens shape, causing incident rays obliquely incident onto a lens to focus at different positions in the image plane. The intensity distribution of the point spread function flares out, creating an asymmetrical comet-like shape. The tail of the comet-like point spread function may be pointing away or towards the center of the image field of view, depending on whether the coma is positive or negative, respectively. Coma can be neutralized using a combination of different lenses with positive and negative coma or can be negated by using an aperture-stop at the proper location.

2.3.4 Chromatic Aberration

Chromatic aberration arises when a lens focuses rays of different color into different focal points. This type of aberration occurs because the refractive index of the lens medium varies as a function of frequency, a phenomenon known as dispersion. Figure 2.10 illustrates an example of chromatic aberration in an imaging system and its effect on the resulting image. Blue, green, and red light are focussed at different positions by the objective lens, and as a result, the microscope image can have a reddish, greenish, or bluish tinge depending on the position of the image plane.

2.3.5 Geometrical Distortions

Geometrical distortions describe aberrations that arise when the transverse magnification, M_T, of a lens varies as a function of off-axis position,

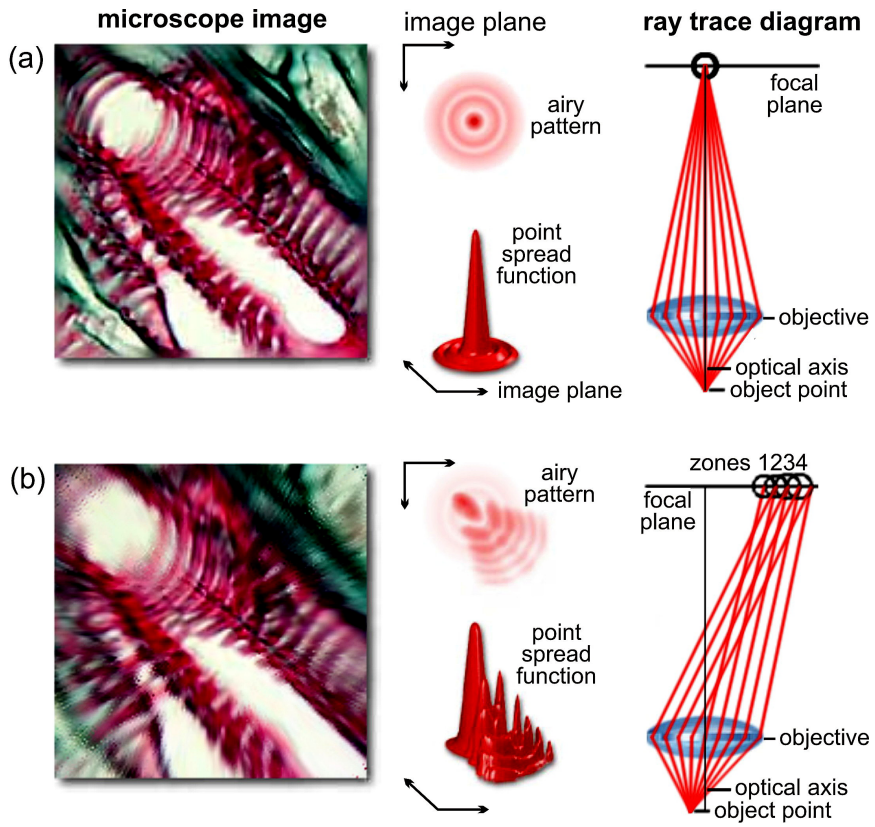

Figure 2.9: Comatic aberration causes smearing of a point source into different zones (1, 2, 3, 4) on the image plane. Point spread function, Airy pattern, and overall image for (a) the case of an aligned imaging system without coma and (b) the case of an unaligned imaging system with coma [19, 20, 22].

yielding distortions in the overall image. Different types of geometrical distortions are illustrated in Figure 2.11. Positive (pin-cushion) distortions are characterized by M_T that increases as a function of axial position, and negative (barrel) distortions are characterized by M_T that decreases as a function of axial position. Simple thick lenses and compound lens systems are prone to geometrical distortions, whereas thin lenses are generally im-

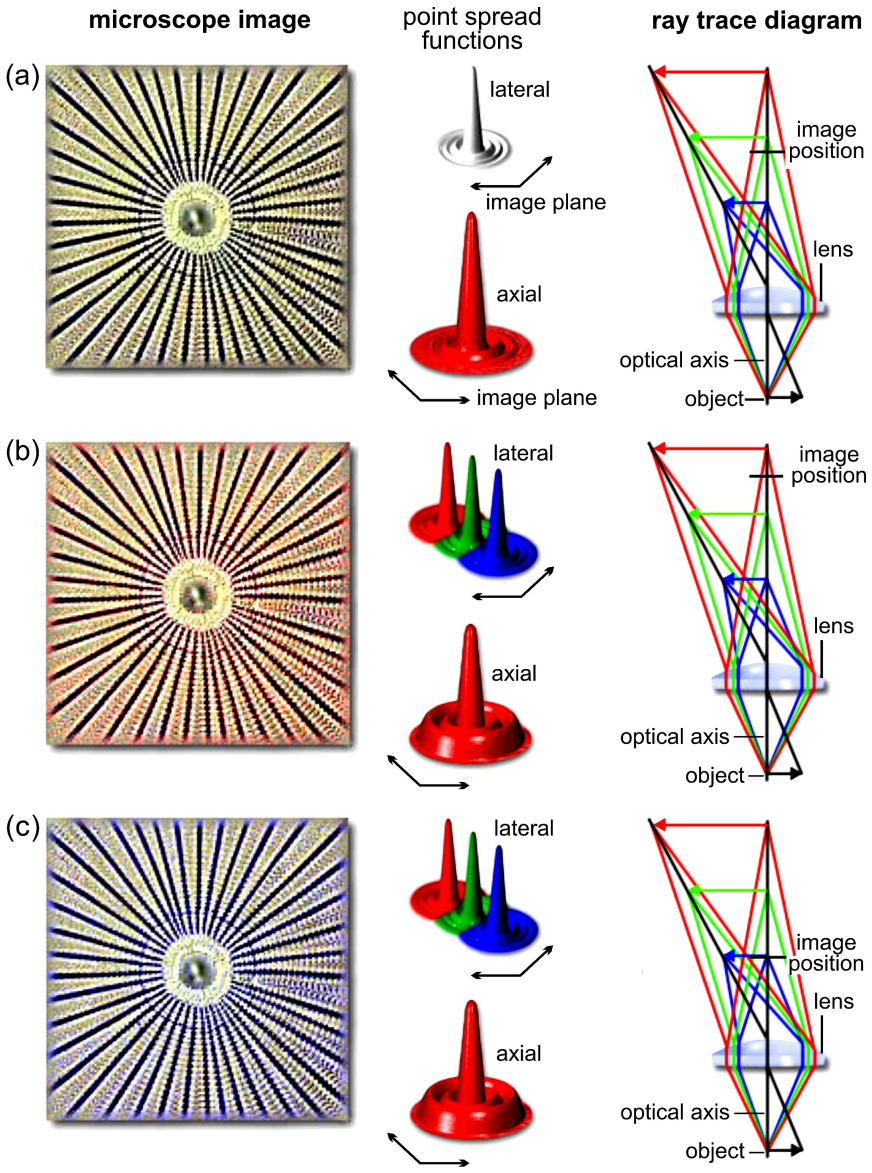

Figure 2.10: Chromatic aberrations with an uncorrected lens, illuminated by a polychromatic (white) point source. The resulting image can have a (a) greenish, (b) reddish, or (c) bluish tinge when the position of the image plane is located at focal points corresponding to the green, blue, red portions of the visible spectrum, respectively [19, 20, 22].

mune to distortions. One method to eliminate geometrical distortions is to cascade positive and negative lenses with respect to a symmetrical aperture stop.

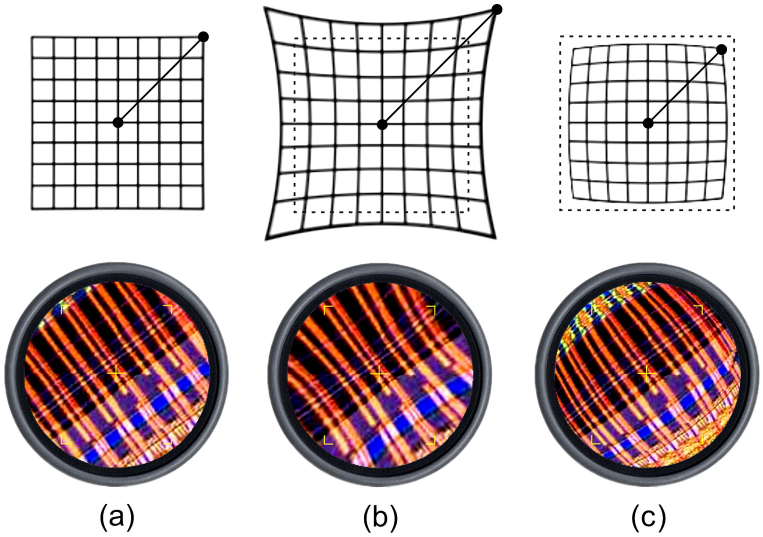

Figure 2.11: Demonstration of geometrical distortion of an image of a grid pattern (top row). (a) The transverse magnification is same for all the image points, irrespective of the distance from the optical axis, yielding an undistorted image. (b) Positive or pin-cushion distortions are evident by larger magnification of the most distant object points from the optical axis. (c) Negative or barrel distortions are evident by the smaller magnification of the most distant object points from the optical axis [19, 20, 22, 27].

2.3.6 Field Curvature

A lens with a curved surface produces an image plane that is also curved. Simple objective lenses fail to simultaneously focus the paraxial (near the centre) and peripheral (near the edge) regions of the object within the field of view. The resulting image is sharp and crisp in either the centre or on the edges, but not both. Inward curvature of the objective lens can be effectively

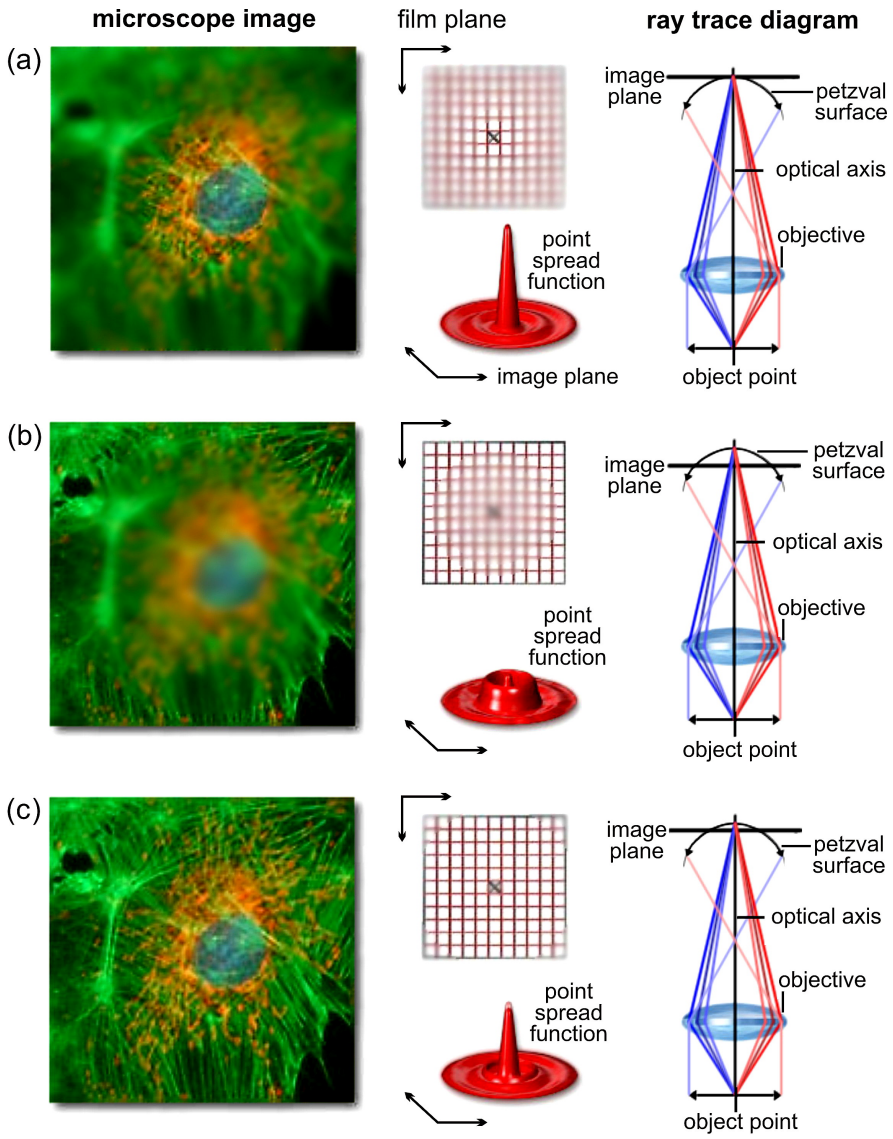

Figure 2.12: Illustration of the effect of field curvature on an image, with the corresponding alterations of PSF and illumination of grid pattern (film plane). At different planes of observation, (a) central portion and (b) edges of the image plane come to sharp focus, making it impossible to distinguish minor details of the image at other regions. (c) represents the best compromise between center and edge focus [19, 20, 22].

nullified by placing a negative field flattener lens near the focal plane, which has little effect on other aberrations. Modern 'plan' or 'plano' objectives are capable of producing sharp image detail from the centre to the edges, but these objective lenses are typically very expensive.

2.4 Optical Aberrations Correction

Advances in glass formation, grinding and manufacturing techniques have resulted in highly complex objective and condenser lens designs, which have nearly eliminated all the aberrations discussed above [17, 25–28]. In this section, we will detail some of the distinguishing features of commercially available objective lens and condensers and review some of the aberration correction features.

2.4.1 Objective Correction

Table 2.1 lists different types of objectives with their corrections for optical aberrations. Achromats, the least expensive, are only partially corrected for chromatic aberration. Fluorites or semi-apochromats are greatly improved over achromats, with better chromatic aberration correction, higher numerical aperture, better resolving power and higher degree of contrast. Apochromats are the best choice for color photomicrography in white light conditions. Achromats, fluorites, and apochromats, however, all suffer from pronounced field curvature [17]. Objectives with correction for flat-field are named 'plan' or 'plano', and are considerably more difficult to fabricate due to the increased number of lenses. For example, typical achromats consists

of five lenses (two lens doublets and a hemispherical lens) in comparison to more complex plan-achromats consisting of nine lens elements (three doublets and three single lenses). Top-of-the-line 'plan-apochromats', corrected for spherical, chromatic and field-curvature aberrations, may contain eighteen to twenty lens elements with proportional increase in cost (upwards to $3000 to $5000 for a single objective), depending on magnification and numerical aperture [26].

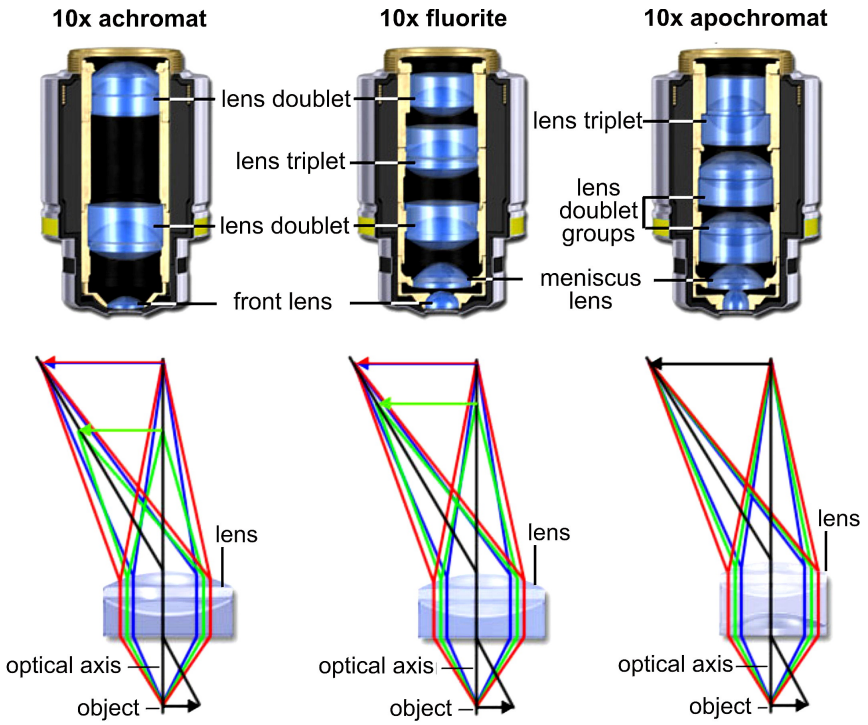

Figure 2.13: Internal lens element combinations (first row) and corresponding ray tracing diagram demonstrating the chromatic correction (second row) incorporated in an achromat (column one), fluorite (column two) and apochromat (column three) objective of 10× magnification [19–22, 28].

Table 2.1: Optical aberration correction for objective lenses

Achromats	• Axial chromatic correction for red and blue • Corrected for spherical aberration in green • Green halo appears in the images for focus chosen in red-blue region • Lack of correction for flatness of field curvature
Fluorites or semi-apochromats	• Improved correction of optical aberration • Corrected chromatically for red and blue, with green focused at a much closer distance • Spherical aberration is corrected for two colors • Suffer from lack of field curvature correction
Apochromats	• Corrected chromatically for three colors (red, green and blue) • Spherical correction for two colors • Suffer from pronounced field curvature
Plan-achromats, Plan-fluorites, Plan-apochromats	• These are achromats, fluorites and apochromats respectively provided with flat-field correction along with other corrections mentioned above • Plan correction is achieved at the cost of significant increase in the number of lens elements

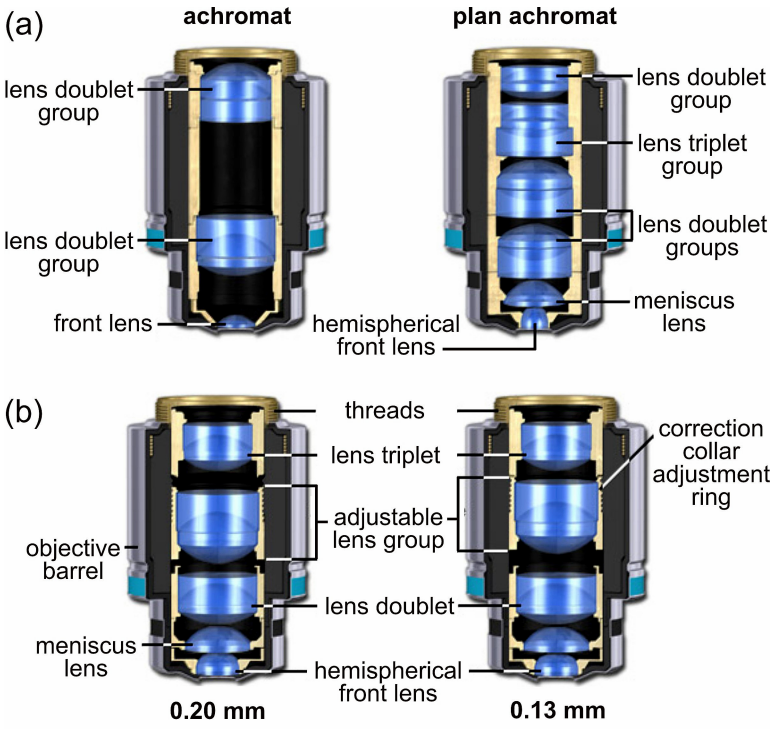

Figure 2.14: (a) Correction for flat-field curvature for a 10× achromat requires insertion of a meniscus lens, a doublet and a triplet lens group into the objective. (b) Correction collar adjustment for different coverslip thickness of 0.20 mm and 0.13 mm to correct for aberrations that are introduced due to the variation of the cover glass thickness and dispersion of the medium between the front lens and the cover glass [19, 21, 22, 28].

2.4.2 Condenser Correction

Different types of condenser corrections are listed in Table 2.2. Abbe condensers possess a wide cone of illumination and are the simplest and least-corrected condenser. Aplanatic and achromatic condensers boast a slightly higher degree of correction. Aplanatic-achromatic condensers have the highest level of correction.

Table 2.2: Optical aberration correction for condenser lenses

Abbe	• Consists of two optical lens elements • Image produced is not sharp and is surrounded by blue and red color at the edges
Achromatic	• Corrected exclusively for chromatic aberration, not for spherical aberration • Typically contains four lens elements • Provides highest attainable numerical aperture of 0.95 without immersion oil
Aplanatic	• Well corrected for spherical aberration in green, but not for chromatic aberration • Featured with five lens elements • Capable of focusing light in a single plane
Aplanatic-Achromatic	• Provides with highest level of correction for both chromatic and spherical aberration • Featured with eight internal lens elements, cemented into two doublets and four single lenses • Best choice for color photomicrography

Chapter 3

Water Droplet Microscopy

Water droplets are an attractive medium to realize lensing elements. Water is transparent over the visible frequency range, ultra-smooth surfaces of a droplet are naturally created through surface tension, and the droplet shape is reconfigurable by either applying pressure or electric fields. Here, we use a water droplet as the magnifying component in a simple microscope operating under either reflection-mode or transmission-mode illumination. A water droplet is created at the end of syringe and then coated with a thin layer of oil to mitigate evaporation. By applying pressure to the water droplet using a metal tip, the shape of the droplet is tuned to yield focusing properties amenable for microscopy. Images captured using the microscope show micron-scale resolution and tunable magnification. The results demonstrate a simple, low-cost, and elegant configuration for realizing a tunable microscope system based on a droplet of water.

3.1 Fluidic Lens Microscopy

A lens is a discrete optical element that causes an incoming beam of light to either converge or diverge. The effect that a lens imparts onto an incident light beam is determined, in large part, by the curvature of the surfaces of

the lens, which then sets its focal length. For a lens constructed from a transparent solid, such as glass, crystal, or plastic, the curvature of the lens surfaces is rigid and its focal length is fixed. Tunability of the focal length then requires a system of lenses, where the effective focal length of the lens system is adjusted by varying the relative positions of the constituent lenses.

There has been growing interest in the development of lenses constructed from fluids [29–32]. The advantage of a fluidic lens, as opposed to a solid lens, is that the curvature of the lens can be easily deformed, meaning that a tunable focal length can be achieved using a single element, and the surfaces of the lens are naturally smooth due to surface tension. The use of a fluid, however, introduces the requirement of systems to provide mechanical stability, prevent evaporation, and manipulate the fluid. To date, fluidic lenses have been implemented in the form of discrete optical elements, consisting of a housing structure to store the constituent fluid and an actuation method to adjust the shape of the fluid. The actuation method is commonly based on the application of mechanical pressure or an electric field to the fluid volume. Fluidic lenses based on the application of electric fields exploit either the electro-wetting effect [31, 33] or dielectrophoresis force [34–38]. Fluidic lenses based on the application of mechanical pressure, on the other hand, exploit the natural deformation of fluids in pressurized environments. Pressure lenses are tuned by either applying a hydraulic or ambient pressure to a fixed fluid volume [32, 39–42] or by changing the volume of fluid [43–50].

Current implementations of fluidic lenses have demonstrated a high degree of stability and control over the shape of the fluid, but require elaborate housing structures [36, 41, 43, 45, 49, 51], in many cases constructed

using multiple micro- or nano-fabrication steps [43, 44]. An alternative and less-explored approach to realizing a fluidic lens is to exploit the existing low-technology methods available to controllably dispense and shape small volumes of fluids. In this work, we explore a fluidic lens constructed from a water droplet attached to a syringe. To mitigate evaporation, the water droplet is encased in a transparent and immiscible silicone oil layer, which also forms the exterior portion of the lens. The droplet is actuated by both applying a pressure with an external tip and varying the volume of the droplet directly through the syringe. The resulting droplet lens possesses large acceptance angles, short focal lengths, and a wide tunability range. A potentially useful feature of this implementation is that the droplet lens can created on demand and discarded after use. We demonstrate the application of the droplet lens as a variable, magnifying component in a microscope operating under both reflection-mode and transmission-mode illumination. Although the droplet lens does not possess the same degree of stability and control as other fluidic lens implementations, it may find usefulness due to the low-cost of implementation, wide availability of requisite equipment, and simplicity of operation.

3.2 Droplet Lens Dispenser and Actuator

We design a fluidic lens based on water droplets controllably dispensed from and attached to the end of a micro-liter syringe (Hamilton 701RN $10\,\mu$L syringe). We establish a coordinate system where the axis of the syringe is oriented along the x-axis (horizontal), gravity is directed along

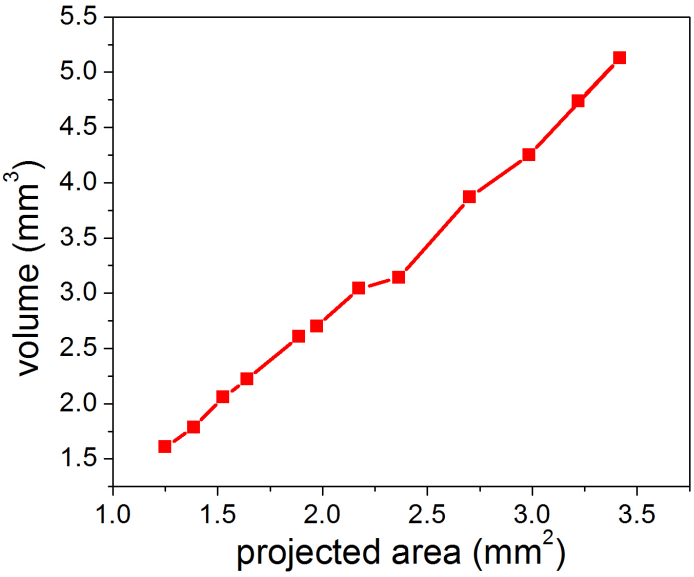

Figure 3.1: Droplet size determination by analysis of images taken of the droplet from horizontal and vertical perspectives. The projected area of the droplet measured from the horizontal perspective as a function of the droplet volume inferred from both perspectives.

the z-axis (vertical), and the optical axis of the lens is oriented along the y-axis. In general, the droplet can be modeled as an ellipsoid with three principle axes a, b, and c, corresponding to the diameters of the droplet along the x, y, and z axes, respectively. The parameters a, b, and c are measured from images of the droplet taken from vertical and horizontal perspectives, where b and c are extracted from the horizontal perspective (yz plane) and a and b from the vertical perspective (xy plane). The volume, V, and horizontal projected area, A, are then given by $V = \pi abc/6$ and $A = \pi bc/4$, respectively. Either the volume or the area can be used as a metric for the droplet size. As shown in Figure 3.1, a positive, monotonic

correlation between the volume and projected area indicates that increases in the droplet volume yield proportional increases of the droplet size in terms of projected area. Throughout the remainder of this paper, the droplet size will be discussed primarily in terms of the horizontal projected area.

A water droplet directly exposed to atmosphere is prone to rapid evaporation which results in shape distortions. To mitigate evaporation, we coat the water droplet in a thin layer of silicone oil. The oil coating is applied by simply dispensing an oil droplet above the attached water droplet. As the oil droplet whisks past the water droplet, a thin protective layer of oil evenly and completely surrounds both the water droplet and a portion of the syringe. As shown in the images in Figure 3.2, addition of the oil coating does not significantly change the overall shape of the water droplet or its transparency, but reduces the evaporation rate of the water droplet by five-fold, from $0.072\,\mathrm{mm}^2/\,\mathrm{min}$ to $0.014\,\mathrm{mm}^2/\,\mathrm{min}$ [Figure 3.2(e)]. Although the oil coating does not completely eliminate evaporation, it does enable a single, millimeter-scale water droplet to last for over an hour. Because the droplet is still attached to the syringe, gradual reduction in the size of the oil-coated water droplet can be compensated by controllably dispensing water from the syringe.

We next study the focussing properties of an oil-coated water droplet as a function of water volume using the configuration depicted in Figure 3.3(a). Light diverging from a single-mode fibre having a $5\,\mu$m core diameter is collimated by the droplet lens and then recorded by a camera placed a distance much greater than the focal length away from the coated droplet.

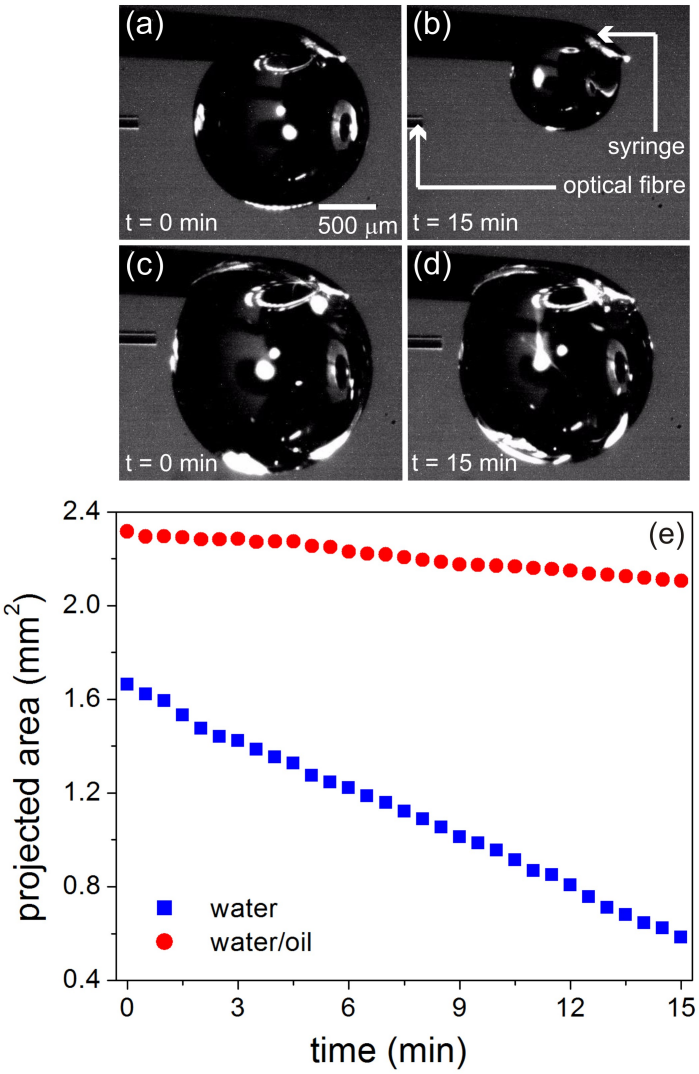

Figure 3.2: Microscope images of a bare water droplet at (a) $t = 0\,\mathrm{s}$ and (b) $t = 15\,\mathrm{min}$. Dispensing a drop of oil over the water droplet results in a thin oil layer surrounding the water droplet. Microscope images of a water droplet with an oil coating at (c) $t = 0\,\mathrm{s}$ and (d) $t = 15\,\mathrm{min}$. (e) The measured projected area of the two types of droplets as a function of time. The bare water droplet has an evaporation rate of $0.072\,\mathrm{mm}^2/\,\mathrm{min}$ and the oil-coated water droplet has an evaporation rate of $0.014\,\mathrm{mm}^2/\,\mathrm{min}$. The evaporation rate depends on the relative humidity and can be further reduced by encasing the setup in a high-humidity chamber. Oil coating the water droplet yields a greater than 5 times decrease in the evaporation rate.

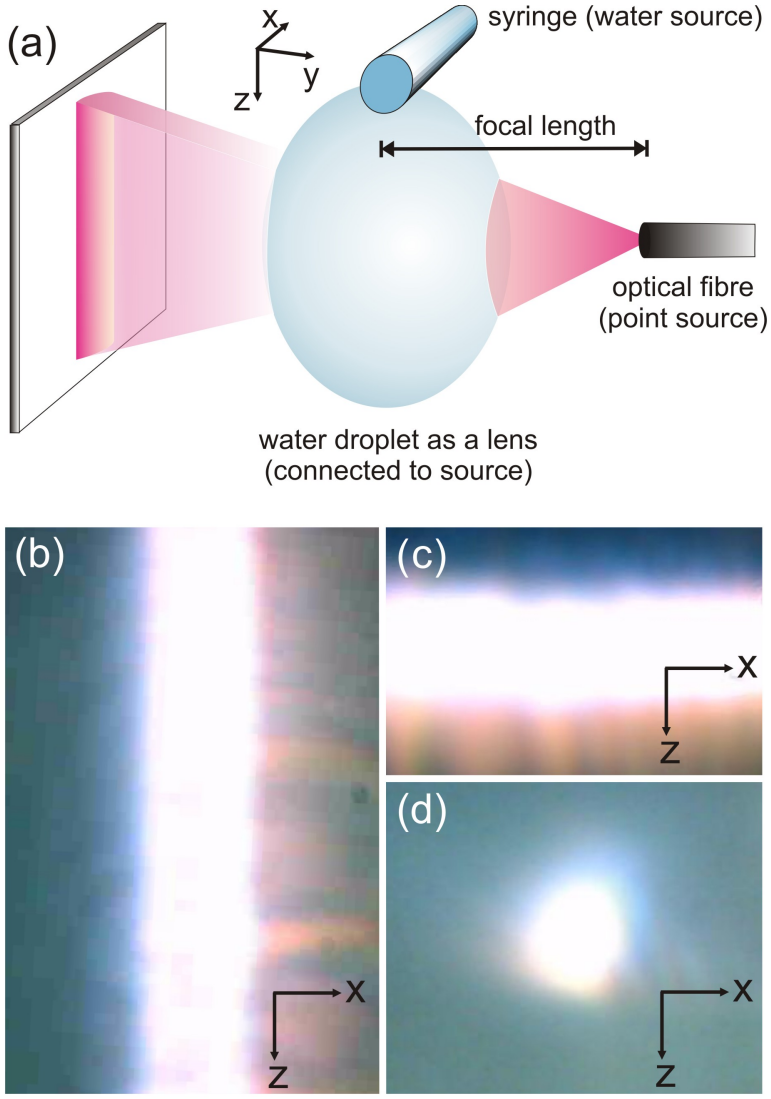

Figure 3.3: (a) Experimental setup to determine the focal distances of the water droplet based on collimation of visible light emitted from an optical fibre. The oil-coated water droplet is attached to a syringe connected to a water reservoir. The focusing properties of the droplet are changed by varying the volume of the droplet. The light emanating from the optical fibre is collimated by the droplet and the far-field image of the light source is collected by a camera at a far distance (much greater than the focal length) from the lens. Typical far-field images indicating (b) horizontal collimation, (c) vertical collimation, and (d) full collimation. The beam shapes are insensitive to the screen position.

The fibre is aligned along the y-axis (optical axis) of the lens to mitigate astigmatism effects. For a given volume, we measure two focal lengths of the lens: a "horizontal" focal length corresponding to the distance from the center of the lens to the fibre tip resulting in a horizontally-collimated beam shape [Figure 3.3(b)] and a "vertical" focal length corresponding to the distance resulting in a vertically-collimated beam shape [Figure 3.3(c)]. The horizontal and vertical focal lengths are generally unequal because the transverse shape of the lens is not symmetric [Figure 3.4(c)]. This asymmetry arises from two competing effects, illustrated in Figure 3.4(d). For smaller droplet volumes, attachment of the droplet along the shaft of the syringe causes elongation of the horizontal diameter a relative to vertical diameter c, yielding an oblate ellipsoidal shape. For larger droplet volumes, the increasing effect of gravity on the droplet causes concurrent elongation of the diameter c and reduction in a, yielding a prolate ellipsoidal shape. As a result, the vertical focal length monotonically increases and the horizontal focal length decreases and plateaus as a function of the increasing droplet size [Figure 3.4(c)]. Due to the competing effects of droplet attachment and gravity, there is only one droplet volume that yields a symmetric transverse shape. When a symmetric transverse shape is achieved, the horizontal and vertical focal lengths are matched, resulting in a beam shape that is fully collimated [Figure 3.3(d)].

To enable greater control over the shape of the droplet for any droplet volume, we incorporate a metallic tip below the end of the syringe that attaches onto the dispensed water droplet. The metallic tip is actuated in three-dimensions, with positioning accuracy on the order of $\simeq 1\,\mu$m, using

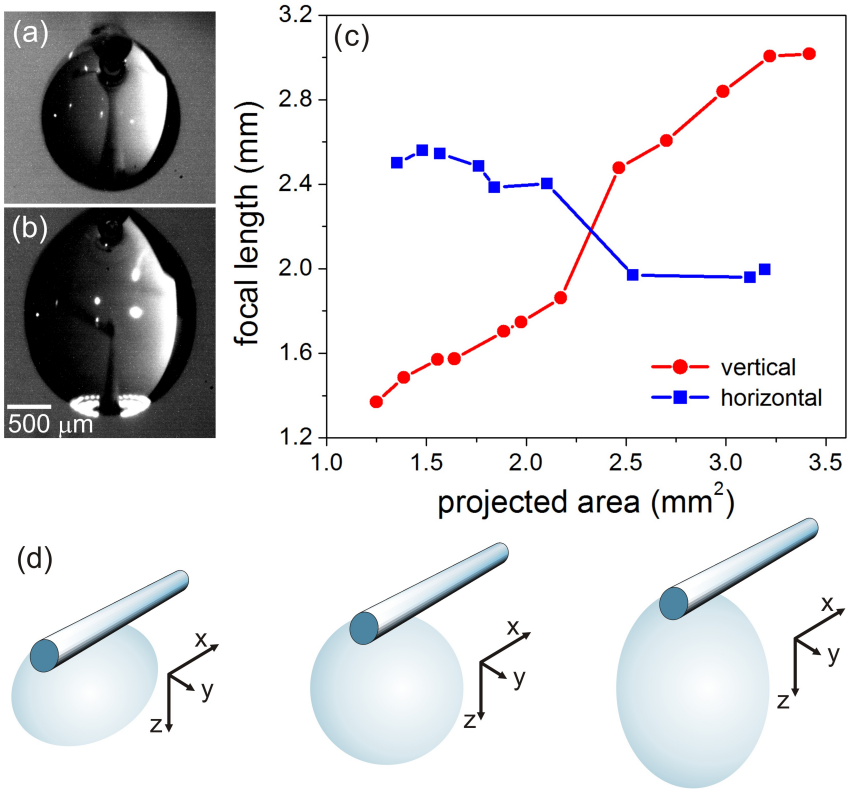

Figure 3.4: (a) and (b) depict images of an oil-coated water droplet attached with the syringe where the size and shape of the droplet has been varied by increasing the water volume. The general shape of the droplet is elliptical. The ellipticity of the droplet is larger for smaller droplets due to adhesion to the syringe and larger droplets due to gravity-induced elongation. Ellipticity in the droplet shape yields disparate focal lengths along the horizontal and vertical directions. (c) Horizontal and vertical focal lengths of the droplet as a function of projected droplet area. For this oil-coated water droplet system, there exists only one droplet size where the horizontal and vertical focal lengths are matched. (d) Illustrations demonstrating the changing shape of the water droplet as a function of volume.

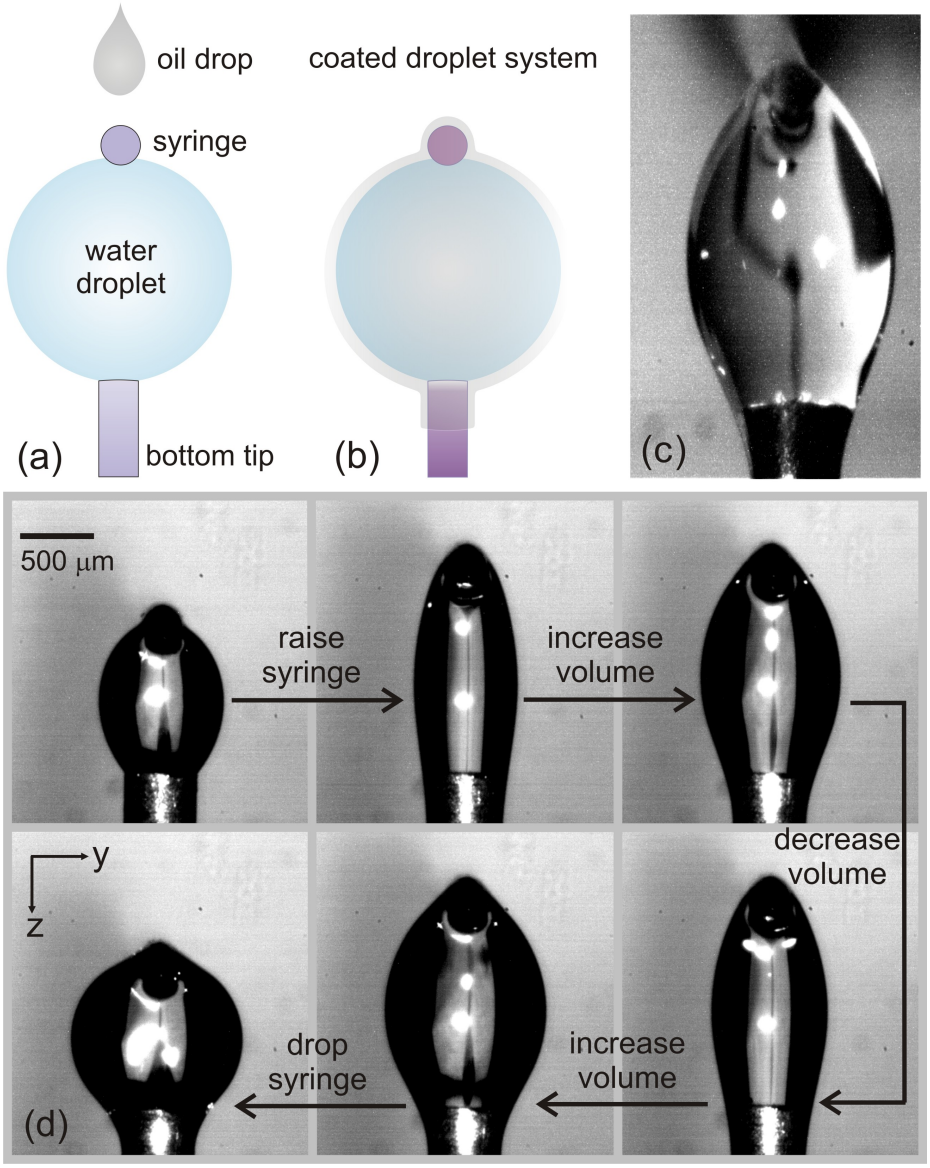

Figure 3.5: Variation of the shape of the oil-coated water droplet system by applying pressure through a bottom tip. A metallic tip is first (a) attached to the bottom of a water droplet. A droplet of oil is then dispensed from a syringe, resulting in (b) an oil-coated water droplet connected to a bottom tip. (c) shows a microscope image of the complete fluidic lens system. (d) Sequence of microscope images of the droplet system demonstrating size and shape reconfiguration by either changing the volume or pressure on the droplet.

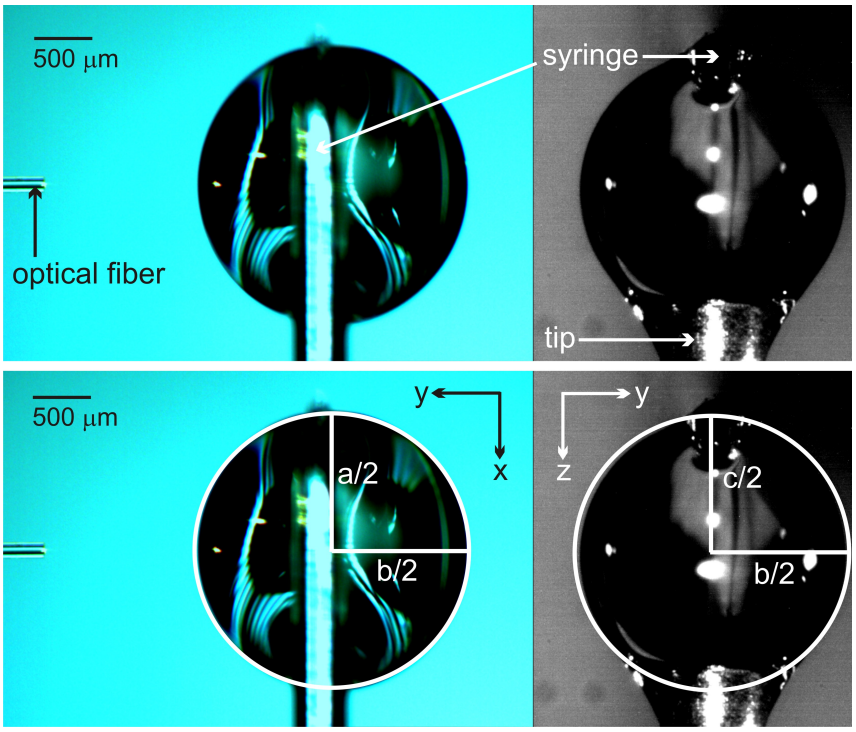

Figure 3.6: Images of a symmetric droplet taken from a vertical perspective (left) and a horizontal perspective (right), where symmetric circles have been superimposed onto the edge of the droplet in the images.

the three-axis mechanical linear stage (Newport ULTRAlign). Inclusion of the bottom tip provides physical support for the weight of the droplet (permitting larger droplet sizes than previously possible without the tip) and enables tuning of the lens curvature, particularly along the vertical direction, by varying the separation distance between the tip and the syringe. An image of a typical fluidic lens resulting from this configuration is shown in Figure 3.5 (c). The sequence of images in Figure 3.5 (d) highlights controllable and reversible alterations of the droplet shape by either changing the droplet volume or varying the tip-syringe separation. In particular, for

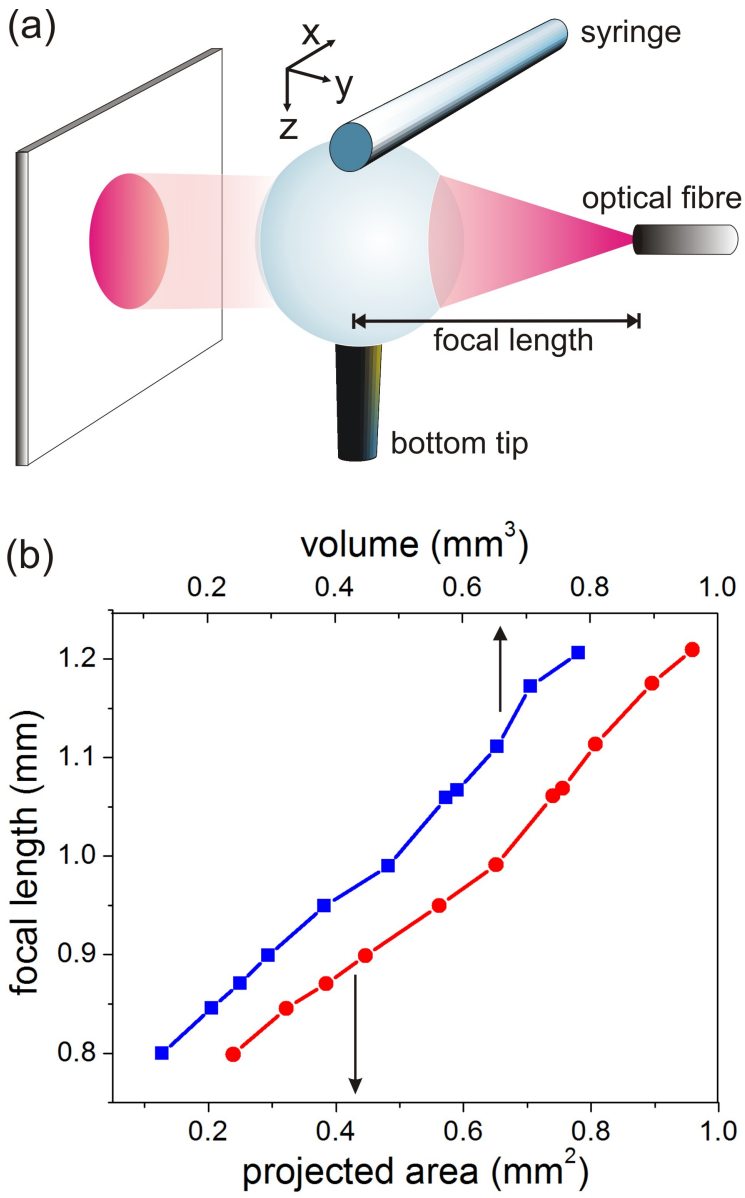

Figure 3.7: (a) Experimental set-up for measuring the focal length of the tip-supported droplet system. By tuning the position of the bottom tip, the shape of the droplet for any volume can be adjusted to achieve complete (horizontal and vertical) collimation of the optical fibre light source. (b) Focal length of the droplet system as a function of droplet volume and projected droplet area.

a given droplet volume, the tip-syringe separation can be varied until a highly symmetric droplet shape is realized (Figure 3.6). The symmetric droplet shape possesses matching vertical and horizontal focal lengths, a basic requirement for application as an imaging lens. Figure 3.7(b) summarizes the focal lengths of a series of droplets, possessing symmetric transverse shapes, created using the modified dispensing and droplet shaping configuration.

3.3 Reflection-Mode Microscope based on a Droplet Lens

We next build a reflection-mode microscope where the oil-coated droplet dispensed from the syringe acts as both the condenser and objective lenses. The microscope configuration is depicted in Figure 3.8. Visible light from a light-emitting diode is directed along the optical axis onto the lens. The lens focuses the incoming light onto a sample and then collects and collimates the reflected light. The collimated beam goes through an aperture with a diameter of 1.38 mm and is then captured by a CMOS camera. The magnification of the microscope is varied by changing the volume of the water droplet and then adjusting the tip-syringe separation until the resulting image is free of distortions. Figure 3.9 (a) depicts representative images of a calibration slide captured by the microscope at various magnification levels. The calibration slide consists of a series of parallel lines, where the pitch spacing between successive lines is 10 μm. The magnification values are measured by comparing the actual size of the sample and the size of the

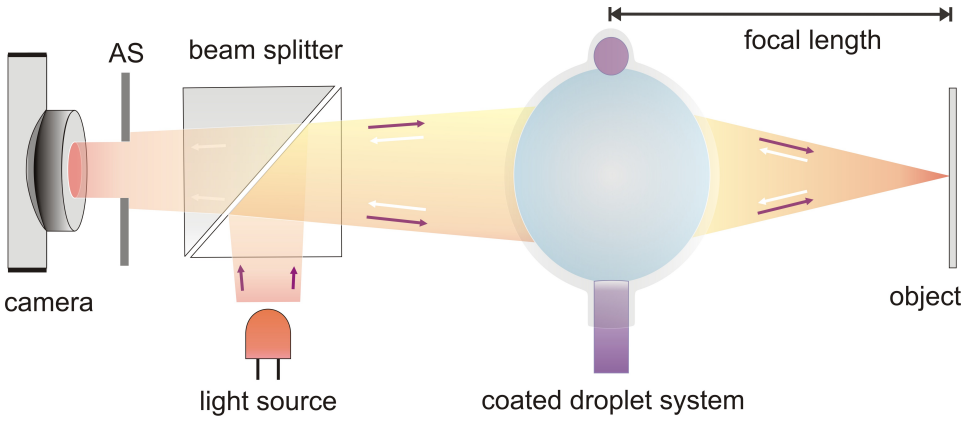

Figure 3.8: Reflection-mode microscope using a fluidic lens composed of the oil-coated water droplet system. In this configuration, the fluidic lens emulates both the condenser and objective lenses found in a conventional optical microscope. A light-emitting diode emits visible light into a beam-splitter, which re-directs the light onto the fluidic lens. The lens focuses the light onto a sample and then collects and collimates the back-scattered light. An image of the focal region is captured using a CMOS camera sensor (Logitech C160 with lens removed).

image of the sample projected onto the CMOS sensor. We position the calibration slide diagonally at an angle of 35° with respect to the horizontal. The diagonal position of the sample enables visualization of barrel [34, 44], pin-cushion [31], or mustache distortions along both the vertical or horizontal directions based on smearing of the lines. Slight overall blurriness of the entire image at larger magnifications (at 43X and 46X) is due to spherical aberrations introduced by the spherical shape of the lens surfaces. As shown in Figure 3.9(b), this particular microscope configuration is capable of magnification values from 37X to 47X, with a corresponding field of view that ranges from 170 μm to 120 μm. It should be noted higher magnification values are possible by using droplets of smaller sizes and lower magnification

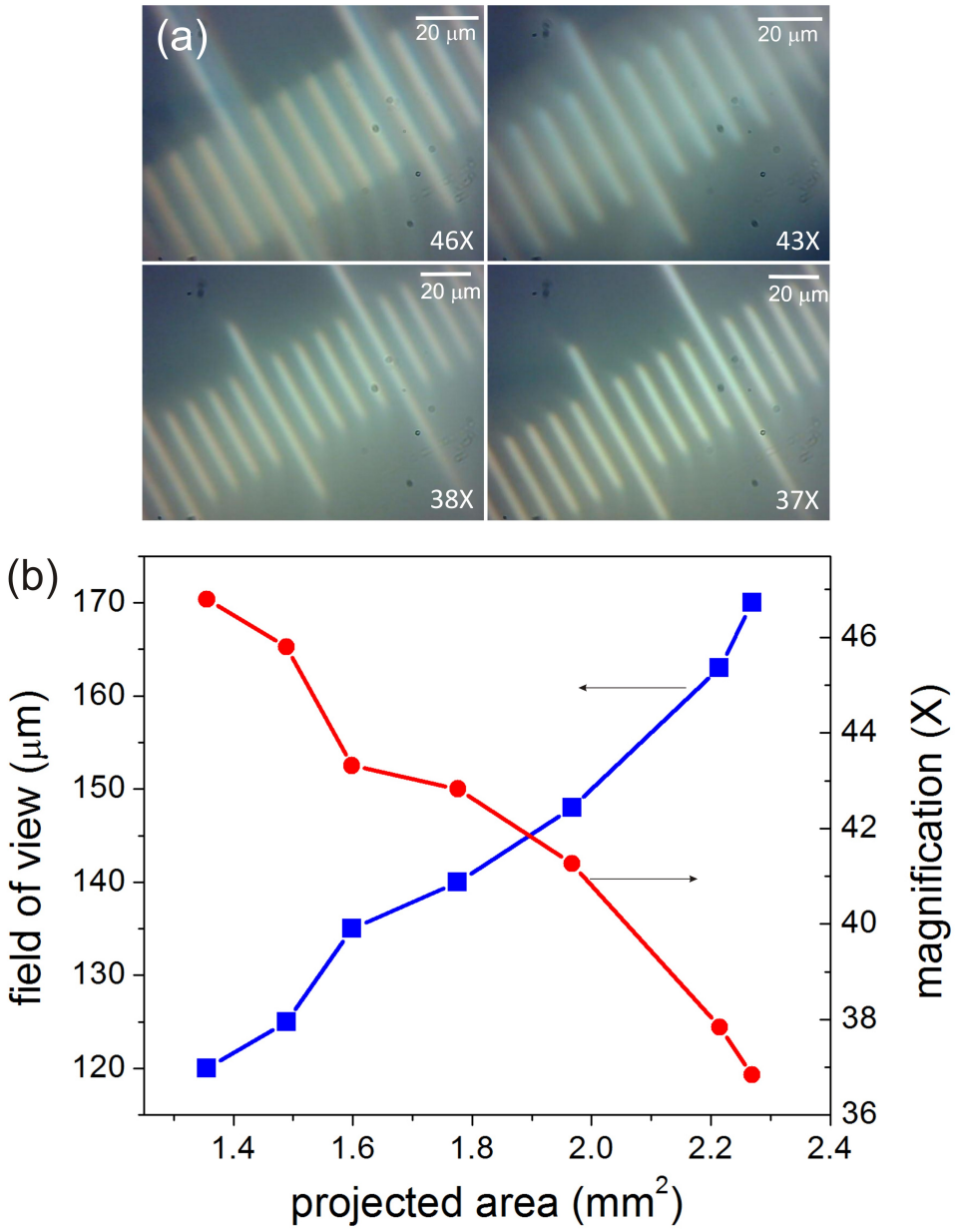

Figure 3.9: (a) Microscope images of a calibration slide captured at various levels of magnification using the fluidic lens microscope. The pitch separation between adjacent lines on the slide is 10 μm. (b) Field of view and magnification of the microscope as a function of projected droplet area.

values are possible by using a larger tip size capable of sustaining larger droplet sizes. One of the reasons for using water as the lens material rather than using a droplet of the non-volatile oil as the lens itself is the high surface tension of water droplet which allows a relatively large sized droplet to remain attached. The focal length of the lens, measured by recording the lens-sample separation yielding the sharpest image, follows the same trend as the focal lengths previously measured using the beam collimation configuration (Figure 3.10). Larger droplet sizes are used in the microscope configuration to accommodate the larger beam size from the light-emitting diode.

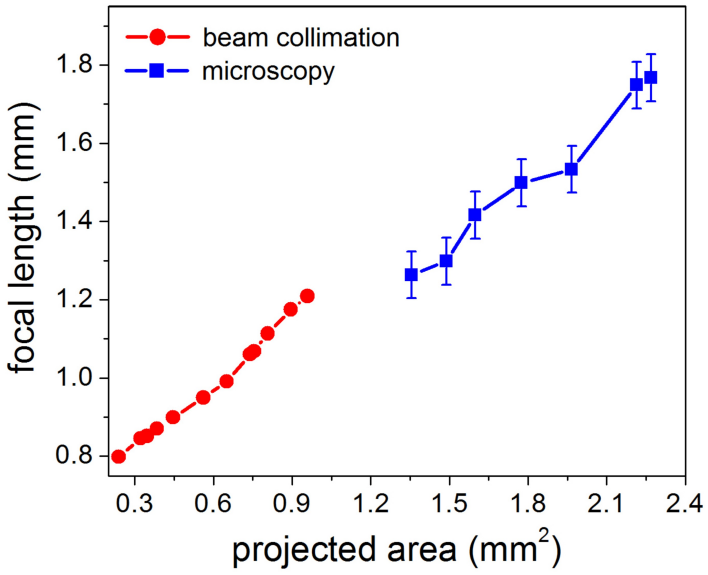

Figure 3.10: Focal length of the oil-coated water droplet lens as a function of projected droplet area measured from the lens-sample separation in the microscopy configuration (blue squares) and the fibre-lens separation in the beam collimation configuration (red circles). The error bars in the measurements in the microscopy configuration account for uncertainty in the position of the sample.

3.4 Transmission-Mode Microscope based on a Droplet Lens

The oil-coated droplet lens is next used as the objective lens in a microscope configuration using transmission-mode illumination. The microscope configuration is depicted in Figure 3.11. Visible light from a light-emitting diode passes through a condenser lens and is focussed onto a sample. Light transmitted through the sample is collected and collimated by the droplet lens. The collimated beam is then captured by a CMOS camera. Figure 3.12 (a) depicts images of various semi-transparent biological samples captured by the microscope at different levels of magnification.

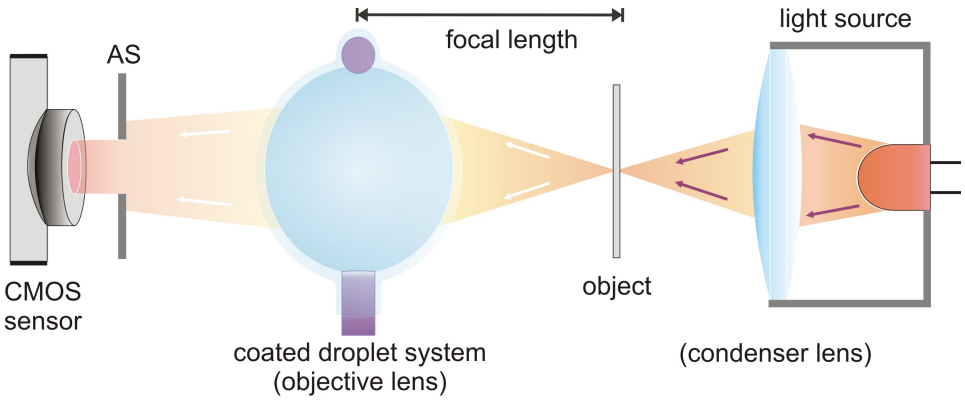

Figure 3.11: Transmission-mode microscope using a fluidic lens composed of the oil-coated water droplet system. In this configuration, a separate lens is used as a condenser lens to illuminate the sample, and the fluidic lens acts as an objective lens. A light-emitting diode emits visible light into the condenser lens, which focuses the light onto the sample. The objective lens collects and collimates the light transmitting through the sample. An image of the focal region is captured using a CMOS camera.

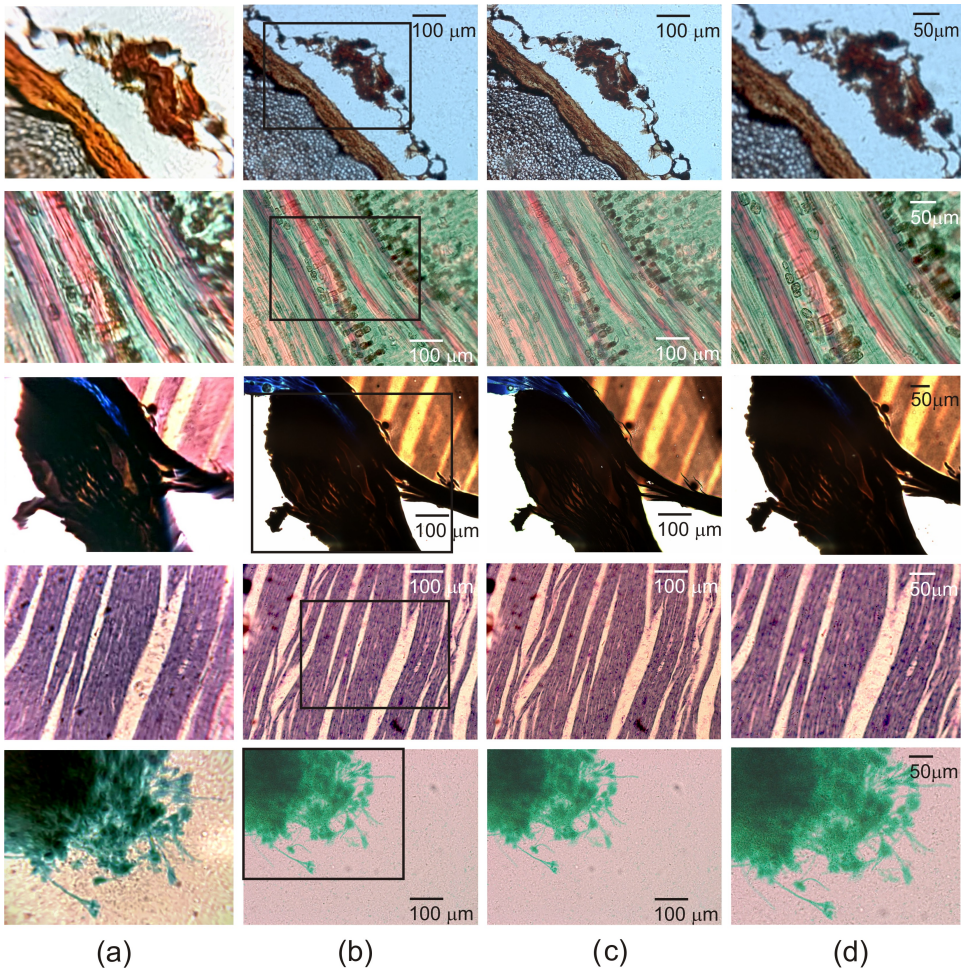

Figure 3.12: Microscope images of spinal cord tissue (first row), basswood stem (second row), cardiac muscle tissue (third and fourth row), and *Penicillium* (fifth row). Column (a) shows the images obtained using the droplet lens in the transmission-mode microscope configuration. Columns (b) and (c) show near-focussed and best-focussed images, respectively, obtained from a conventional laboratory-grade microscope (Zeiss AxioImager) using a 20× objective lens. Column (d) shows cropped images of the highlighted region in the near-focussed images, which matches the region imaged by the droplet lens.

Slight blurriness near the edges of the images are attributed to Petzval field curvature effects [27] (as opposed to spherical aberration effects observed in the reflection-mode images in Figure 3.9). To qualitatively access the performance of the droplet lens, two sets of microscope images are captured by a conventional laboratory-grade microscope (Zeiss AxioImager) using a 20× objective lens: best-focussed images in which the sample is positioned at the focal plane and near-focussed images in which is sample is positioned slightly outside of the focal plane [Figures 3.12 (c) and (d)]. Images captured using the droplet lens have comparable micron-scale resolution and image quality to those obtained by the conventional microscope. The level of detail captured by the droplet lens does not match that of the best-focussed images, but is more comparable to that of the near-focussed images. Nonetheless, the imaging capabilities of the droplet are impressive considering the relative simplicity of our implementation.

3.5 Modeling the Optical Properties of the Droplet Lens

We model the droplet as a thick lens with geometrical parameters extracted from the images of the droplet [Figure 3.13]. The thickness of the lens, d, is the droplet diameter b along the optical axis and the height of the lens (or total aperture size) is $2r$, which is approximately half of the total tip-syringe separation. We extract the radii of curvature by fitting the shape of the front and back surfaces of the droplet, captured in images of the droplet taken from a horizontal perspective, with circles of radii R_1 and

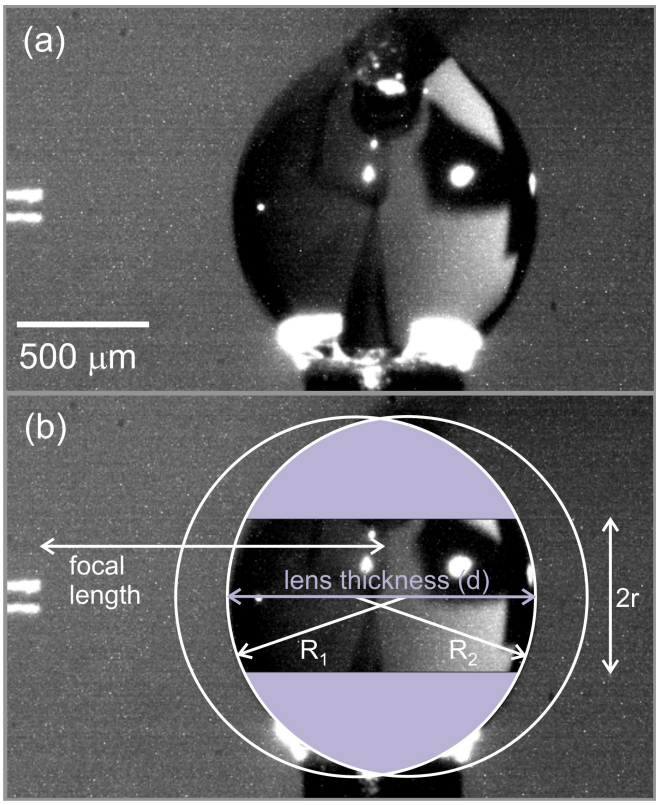

Figure 3.13: (a) Image of an oil-coated water droplet (taken from the horizontal perspective) adjacent to an optical fibre light source. The separation between the bottom tip and syringe has been tuned to reduce the ellipticity in the droplet shape. (b) depicts the procedure to extract the geometrical parameters of the lens for theoretical analysis. The two curved surfaces of the droplet are fitted to circles with radii of curvature of R_1 and R_2. d is the thickness of the lens and $2r$ is the aperture size of the lens.

R_2, respectively, and then scaling the pixel sizes in the image to real dimensions. The transverse shape of the lens is symmetric (as observed from the images of the droplet taken from both horizontal and vertical perspectives [Figure 3.6] and further supported by observations of full beam collimation

and distortion-free imaging), meaning that the parameters d, $2r$, R_1, and R_2 are the same regardless of the direction that the lens is viewed. The focal length is measured with respect to the center of the lens.

Figure 3.14 (a) illustrates an idealized biconvex thick lens created using geometrical parameters extracted from images of the water droplet. The effective focal length, f_h, of the thick lens for paraxial approximation can be calculated [27] as

$$\frac{1}{f_h} = (n_l - 1)\left[\frac{1}{R_1} - \frac{1}{R_2} + \frac{(n_l - 1)\,d}{n_l R_1 R_2}\right]. \tag{3.1}$$

Values of f_h are determined with respect to the principal planes of the lens (as shown in Figure 3.14), which are located at distances

$$h_1 = -\frac{f_h\,(n_l - 1)\,d}{R_2 n_l} \tag{3.2}$$

and

$$h_2 = -\frac{f_h\,(n_l - 1)\,d}{R_1 n_l} \tag{3.3}$$

from the vertices of the front and back surfaces, respectively. Given the symmetric biconvex lens shape in our experiments where $|R_1| = |R_2| = R$ and hence $|h_1| = |h_2| = h$, f_h is related to the focal length measured from the center of the lens f_p by

$$f_p = f_h + \left(\frac{d}{2} - h\right). \tag{3.4}$$

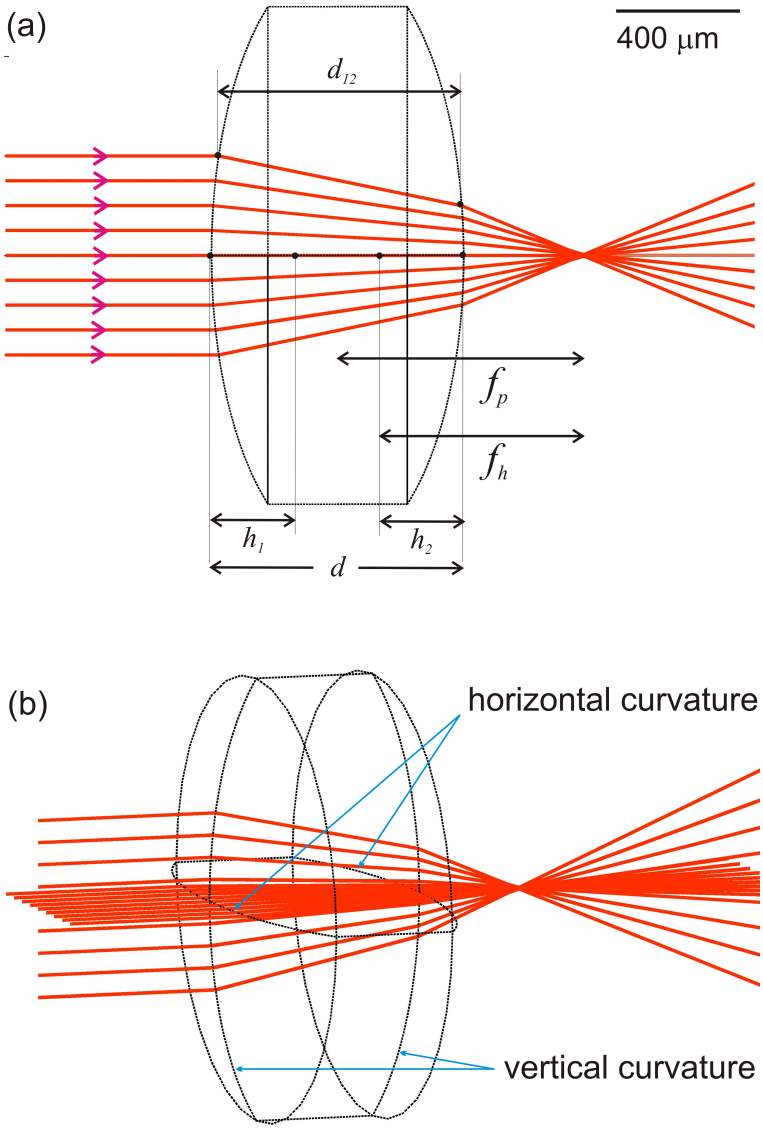

Figure 3.14: Schematic of an idealized thick lens constructed using the geometrical parameters of the fluidic lens. (a) Two-dimensional and (b) three-dimensional perspective of the calculated ray trajectories of a collimated beam incident at normal incidence onto the thick lens. The focal length corresponds to the distance from the center of the lens to the convergence point of the rays.

For each droplet size, we extract the geometrical lens parameters d, $2r$, R_1, and R_2 from the images taken of the droplet from the vertical and horizontal perspectives. The focal length of the droplet is determined by analytical calculations under the paraxial approximation (Eqs. 3.1 and 3.4) and a ray tracing simulation based on the transfer-matrix method. Figures 3.14(a) and (b) show ray tracing simulation results of a collimated input beam incident onto a lens created using realistic parameters extracted from images of a droplet lens. The ray tracing simulations are conducted for collimated illumination where the aperture fill factors (corresponding to the ratio of the illuminated aperture to the total lens aperture) are 30%, 70% and 100%. The results of the ray tracing simulations for the three fill-factor test cases are depicted in Figures 3.15 (b), (d), and (f). For 30% fill factor, the focal length measured from the ray tracing simulations simply corresponds to the distance from the center of the lens to the well-defined convergence point of the rays with the optical axis. For 70% and 100% fill factors, the rays no longer converge at a single point due to the strongly refracted rays incident at distances further from the optical axis and the focal length instead corresponds to the distance from the center of the lens to point where the diameter of the cone formed by the rays is minimum, known as the circle of least confusion, $\sum_{\mathrm{LC}}$. Figures 3.15 (a), (c), and (e) compare the focal lengths calculated under the paraxial approximation and simulated with the ray tracing simulation with the focal lengths measured via beam collimation. Analytical calculations using the paraxial approximation and the ray tracing simulations for 30% fill factor consistently over-estimate the experimentally-measured focal lengths for all droplet sizes. Increasing the

fill factor decreases the focal length values extracted from the ray tracing simulations. Ray tracing simulations using a 70% fill factor yield focal length values most closely matching the experiment.

We next compare the calculated focal lengths to the focal lengths measured using the microscope configuration [Figure 3.16]. The microscope includes an aperture stop that restricts the beam size to a diameter of 1.38 mm. When the droplet size exceeds the aperture stop dimension, the focal length measurements more closely match those calculated under the paraxial approximation. As the droplet size decreases to less than the aperture stop dimension, the paraxial approximation fails and the focal lengths are better modeled using ray tracing simulations with high fill factor. Spherical aberrations are thus expected to be lower for larger droplets and higher for smaller droplets, a trend consistent with the microscope images shown in Figure 3.9. The sharpest images are obtained at lower magnifications (using larger droplets) and the blurriness increases at higher magnifications (using smaller droplets). It should be noted that the focal lengths measured using the beam collimation configuration for all droplet volumes are consistent with ray-tracing simulations using a 70% fill factor. Assuming that the beam emanating from the fibre has a small divergence angle, proportionality between the droplet aperture size and focal length yields an approximately constant fill factor. Overall consistency between the focal lengths measured using the beam collimation and microscopy configurations and the calculated focal lengths suggests that refraction due to the thin oil coating surrounding the water droplet does not significantly influence the focussing properties of the lens.

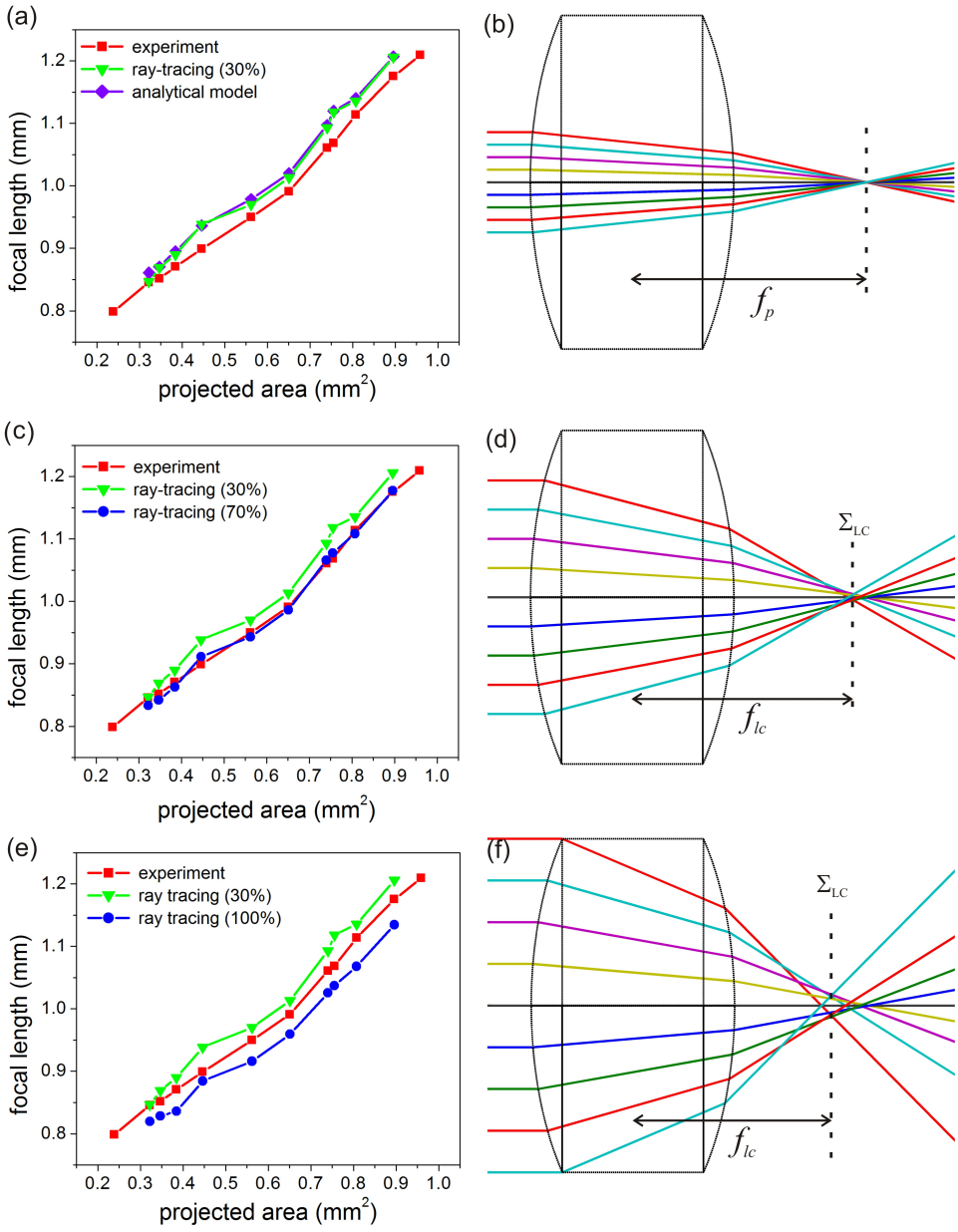

Figure 3.15: Comparison of focal lengths measured using the beam collimation configuration to focal lengths calculated using the analytical model under the paraxial approximation and the ray-tracing simulation using (a) 30%, (c) 70%, and (d) 100% fill factors. The results of the ray tracing simulations using (b) 30%, (d) 70%, and (e) 100% fill factors.

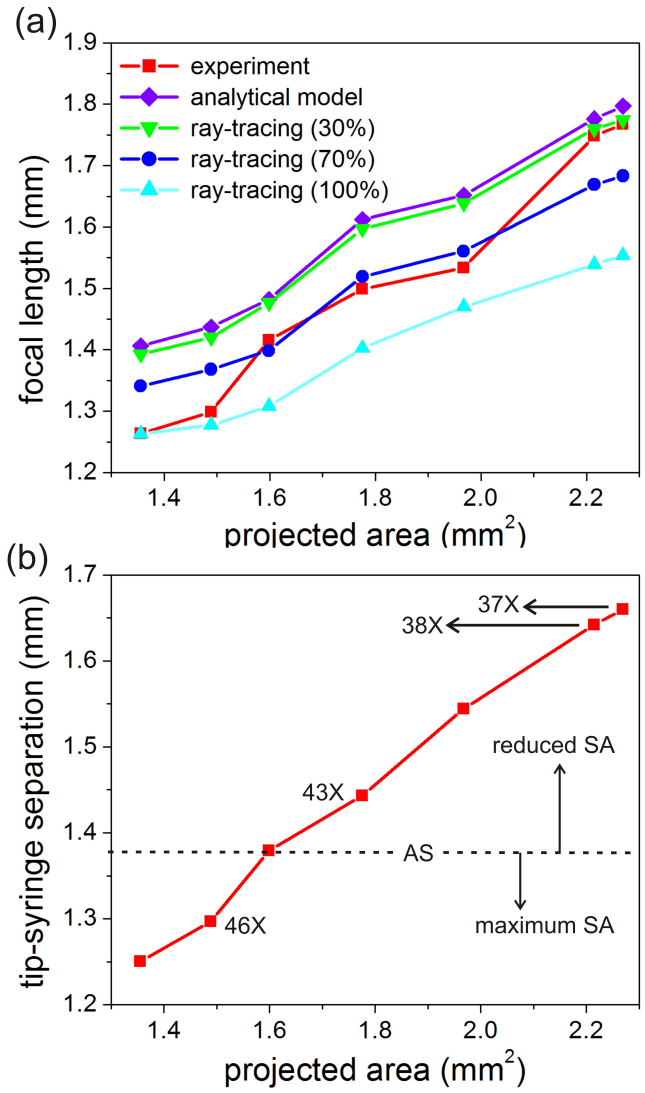

Figure 3.16: (a) Comparison of the focal lengths measured using the microscope configuration to focal lengths calculated using the analytical model under the paraxial approximation and the ray-tracing model using various fill factors. (b) Tip-syringe separation of the lens versus the droplet size. The size of the aperture stop is shown by the dotted grey line. For tip-syringe separations exceeding the aperture size, the corresponding images have reduced spherical aberrations (denoted as SA in the plot), and for tip-syringe separations less than the aperture size, the images have greater spherical aberrations. The magnification provided by various droplet sizes are labeled, corresponding to the microscope images shown in Figure 3.8.

3.6 Limitations

The most significant limitation of building an imaging system based on a suspended droplet is lack of mechanical stability. Changes in the shape of the droplet due to ambient vibrations and gradual reduction of the droplet size due to evaporation both cause distortions in the captured image. Ambient vibrations can be reduced by using vibration dampening stages. Evaporation has been mitigated, but not eliminated, by coating the droplet with a thin layer of silicone oil. Further reduction in the evaporation rate of the droplet can be achieved by housing the system in a sealed and humidity-controlled environment, or housing the entire syringe and droplet system in an immiscible fluidic environment. Another limitation of our implementation is alignment sensitivity due to fluctuations in the optical axis as the droplet size changes. This effect has been mitigated by using a light-emitting diode with a wide emission angle and a CMOS sensor area larger than droplet size, both of which reduces the sensitivity of the image to the optical axis location, but could be further reduced by developing an alignment system that automatically adjusts the position of optical elements with respect to the size of the droplet.

3.7 Summary

In conclusion, we have explored a novel, low-technology method to implement a fluidic lens using low-cost and widely available techniques to dispense and shape small volumes of fluids. The fluid lens consists of a single droplet of water attached to the end of a micro-liter syringe. The water droplet is

coated with a layer of silicone oil which forms the outer portion of the lens and mitigates rapid evaporation of the droplet. The shape and size of the droplet are tuned by applying an external pressure to the droplet through a tip and directly injecting water into the droplet through the syringe. A unique feature of this fluidic lens implementation is that the lens can be created on demand and can be discarded after use with little waste of materials. We have characterized the focussing properties of the droplet lens as a function of the droplet size and used the droplet as the objective lens in both reflection-mode and transmission-mode microscope configurations. The droplet lens is capable of micron-scale resolution imaging, wide tunability by varying the droplet volume, and image quality comparable to, but noticeably less than, that obtained by conventional laboratory-grade microscopes. Although our low-technology implementation lacks the mechanical stability and degree of control of recently explored fluidic lens implementations, it may be useful in resource-limited regions due to the low cost of implementation, wide accessibility of the requisite materials, and relative simplicity of operation.

Chapter 4

Fibre-Addressable Surface Plasmon Resonance Chip Using Optically Matched Fluid

Surface plasmons are transverse-magnetic (TM) polarized electromagnetic waves that are coupled with free electron density oscillations at the interface of a metal and a dielectric medium [52–54]. Surface plasmon resonance (SPR) describes a condition where light couples efficiently into surface plasmons, light waves that propagate along the surface of a metal. A SPR device is a type of optical sensor that exploits the sensitivity of surface-plasmon coupling to the dielectric environment adjacent to a metal surface. A common SPR device configuration consists of a substrate with a metallic layer, an external light source, optical components to polarize and guide light, a coupling device (typically a prism) to convert light into surface plasmons, and a light detector. SPR devices have found niche application as non-destructive, label-free biochemical sensors [55, 56].

There are a couple of limitations with existing SPR device architectures. First, the requirement of many external components restricts the miniaturization of SPR devices. Second, SPR devices require expensive optical elements, such as prisms, which drives up the cost and makes single-use application infeasible. In an effort to overcome these limitations, we design, fabricate, and test a SPR device architecture that is fibre-addressable, does not require a discrete coupling structure, and integrates the light delivery and polarization control onto the a single flexible substrate. Our SPR device consists of a thin gold layer deposited on a clear plastic sheet, which is then optically connected from the bottom surface onto a plastic linear polarizer sheet. Two cleaved fibres, one to collect the input light and the other to collect the output light, are then optically attached to the SPR chip. The angles of the collection fibres are tuned so that visible light incident onto the gold film from the bottom of the chip couples to surface plasmons on the other side of the gold film. Because the SPR device is constructed entirely from widely-available and inexpensive components, it has the advantages of low-cost and amenability to single-use applications.

4.1 Surface Plasmon Resonance: Wavevector Matching Condition

Surface plasmon resonance occurs when the wavevector of light matches the surface plasmon wavevector [57]. For an interface between a dielectric medium, characterized by a permittivity ϵ_1, and metallic medium, charac-

terized by a permittivity ϵ_2, the surface plasmon wavevector is given by

$$k_{SPP}(\omega) = \frac{\omega}{c}\sqrt{\frac{\epsilon_1(\omega)\,\epsilon_2(\omega)}{\epsilon_1(\omega) + \epsilon_2(\omega)}} \tag{4.1}$$

where ω is the frequency and c is the speed of light in vacuum. The wavevector of light in the dielectric medium, on the other hand, is given by

$$k_d = \frac{\omega}{c}\sqrt{\epsilon_1(\omega)}, \tag{4.2}$$

which, for $\epsilon_1 \geq 1$, is always less than k_{SPP}. Inequality between the surface plasmon wavevector and the light wavevector precludes wavevector matching. This is shown in Figure 4.1(a), which plots the surface plasmon wavevector for the representative case of an air-Ag interface and the wavevector of free-space light at grazing incidence ($\theta = 90°$) on the interface. The free-space light wavevector forms a straight line and is commonly known as the "free-space light line". At low frequencies, the surface plasmon wavevector is similar to the free-space light line, but as the frequency increases, the wavevector departs from the free-space light line and increases towards an asymptotic limit. In general, the wavevector matching condition cannot be achieved because the surface plasmon wavevector lies to the right of the light line, for any incidence angle up to the limiting case of grazing incidence.

Surface plasmon resonance via wavevector matching requires either an increase in the light wavevector with respect to a fixed surface plasmon wavevector or a decrease in the surface plasmon wavevector with respect to a fixed light line, both of which shift the relative positions of the light

wavevector and surface plasmon wavevector so that regions of overlap are possible. This requires at least three distinct media: a metallic medium, a dielectric medium of lower refractive index and another dielectric medium of higher refractive index. In the simplest configuration where a metallic medium is sandwiched on both sides by the two types of dielectric media, there are at least four types of waves that are possible: two light waves, one in each dielectric media, and two surface plasmon waves, one at each of the two interfaces of the metallic medium. Figure 4.1(b) plots dispersion diagrams of the possible light and surface plasmons waves for the representative case of an Ag medium sandwiched by air and glass. Although wavevector matching is not possible between light and surface plasmons associated with the same dielectric medium, wavevector matching is possible between light in glass and surface plasmons at the air-Ag interface [53].

Wavevector matching between light incident onto a metal surface from an optically denser medium and surface plasmons at the interface between a metal and an optically rarer medium can be achieved by either tuning the incidence angle (known as angle modulation) or tuning the wavelength of light (known as wavelength modulation). Both angle modulation and wavelength modulation provide a means to shift the incident light wavevector until it matches with the surface plasmon wavevector, and are highlighted in Figure 4.2. Wavevector matching results in a drop in the reflectivity from the metal surface, which can be mapped as a function of angle or wavelength. Representative SPR reflectivity curves are shown in Figure 4.3, for the case of a silver medium sandwiched by a denser dielectric medium (substrate) of

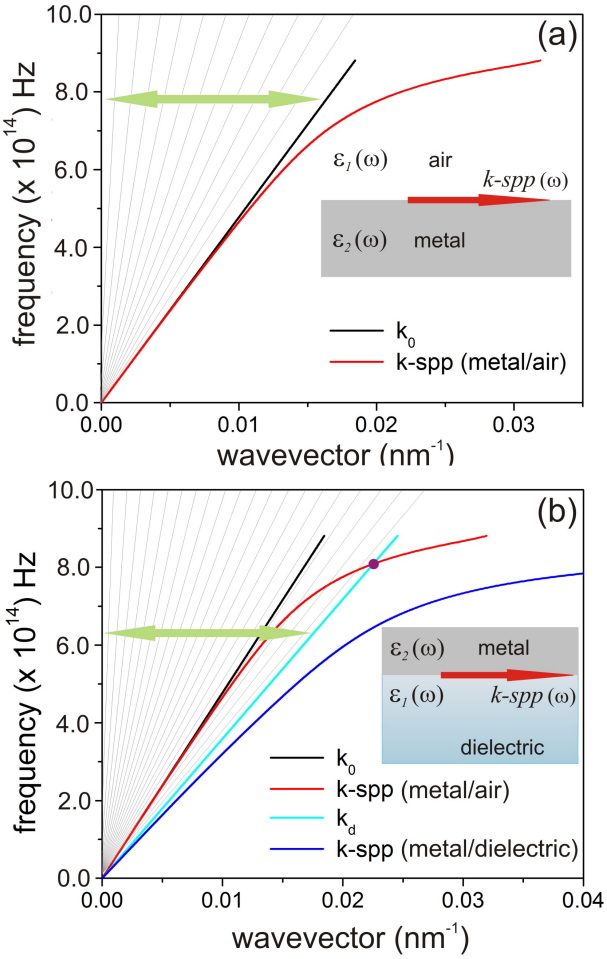

Figure 4.1: Dispersion relation diagrams illustrating the wavevector matching condition required for light coupling into surface plasmons on a planar air-metal interface. The metal is assumed to be Ag. (a) depicts the real part of surface plasmon wavevector (red line) at an air-Ag interface and the component of the free-space light wavevector (black line) projected onto the interface at grazing incidence $\theta = 90°$. The gray lines depict the component of the free-space light wavevector projected onto the interface for intermediate incidence angles. (b) depicts the real part of surface plasmon wavevector (red line) at an air-Ag interface and the component of the light wavevector in a dielectric (cyan line) projected onto the interface at grazing incidence $\theta = 90°$. The gray lines depict the component of the light wavevector in a dielectric projected onto the interface for intermediate incidence angles. Note that wavevector matching is possible between the surface plasmon at an air-metal interface and the light wavevector in a dielectric.

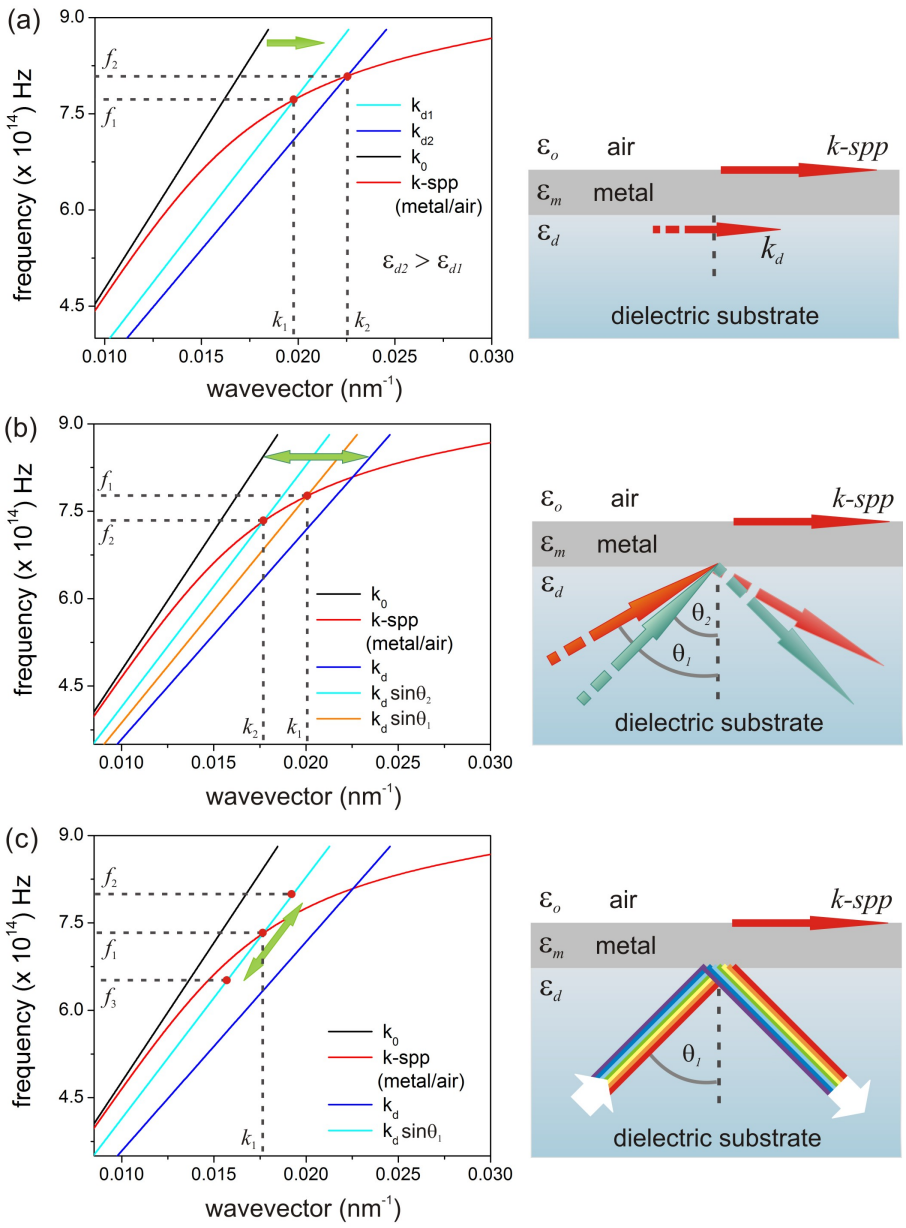

Figure 4.2: Illustration of design parameters tuning in order to achieve required wavevector matched condition. Alteration of the (a) permittivity of higher index dielectric, ϵ_d and (b) angle of incidence, θ into the dielectric makes surface plasmon excitation possible at a desired frequency by shifting the light line. Wavevector matching condition can also be satisfied by (c) tuning frequency of incident light, f along a particular light line.

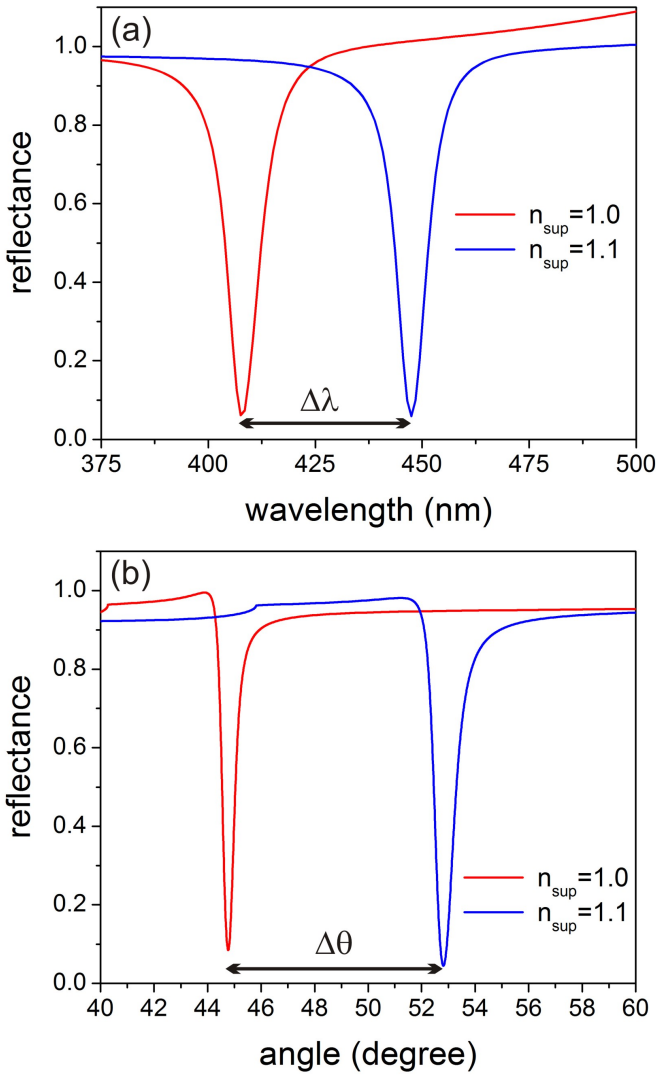

Figure 4.3: Drop in the intensity of reflected light due to surface plasmon resonance. (a) and (b) demonstrates surface plasmon resonance curve for the detection of any slight change in superstrate refractive index through wavelength modulation and angle modulation respectively, $\Delta\lambda$ and $\Delta\theta$ depicts the corresponding shift in the resonance curve due to the change in superstrate medium.

refractive index 1.5 and a rarer dielectric medium (superstrate) of variable refractive index ranging from 1.0 to 1.1. SPR sensors exploit the sensitivity of the position of the reflectivity dip on the dielectric environment adjacent to the metal surface. As the dielectric constant of the superstrate is changed from 1.0 to 1.1, the position of the reflectivity dip shifts to higher angles for the case of angle modulation and longer wavelengths for the case of wavelength modulation.

4.2 Optical Coupling Configurations to Measure Surface Plasmon Resonance

A common method to optically couple to surface plasmons uses the Kretschemann configuration [58, 59]. As shown in Figure 4.4(a), the Kretschemann configuration consists of a thin metal film deposited on a high-refractive-index prism. Light, typically from a laser source, is polarized and directed onto the metal film from the prism side. The prism region below the metal film is known as the substrate, and the region above the metal film is known as the superstrate. For a sufficiently thin metal film, light incident onto the film from the prism side evanescently tunnels through the film, enabling light on the prism side to couple to surface plasmons on the superstrate side. When the incidence angle is tuned so that wavevector matching is achieved between incident light and surface plasmons on the superstrate side, efficient surface plasmon coupling is achieved and the intensity of the light reflected from the film diminishes. The external angle (measured with respect to the

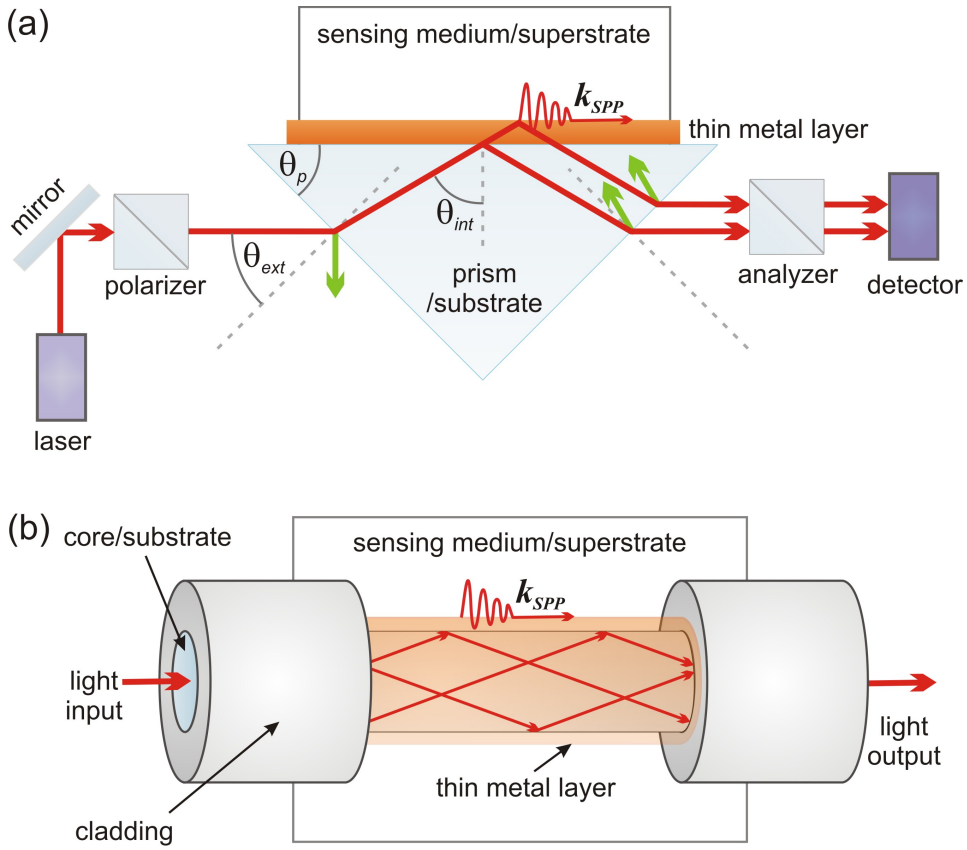

Figure 4.4: (a) Kretschemann configuration and (b) optical fibre configuration to optically coupling to surface plasmons. In both configurations, light incident onto a thin metal film from an optically denser dielectric medium (labeled the "substrate") couples into surface plasmons on the interface between the metal film and the optically rarer dielectric medium (labeled the "superstrate").

normal to the prism face) is related to the internal incidence angle by

$$\theta_{int} = \arcsin\left(\frac{n_a}{n_p}\sin\,\theta_{ext}\right) + \theta_p, \tag{4.3}$$

where θ_p is the angle from the prism/metal interface to adjacent side, n_p and n_a are the refractive index of the prism material and free space respectively.

Another widely-used method to optically couple to surface plasmons uses a coated optical fibre [60, 61]. As shown in Figure 4.4(b), the optical fibre configuration consists of a thin metal film deposited onto the exposed core of an optical fibre. In the region of the exposed core, light guided within the optical fibre interacts with the thin metal film. Optical coupling to surface plasmons from the fibre core to the other side of the metal film occurs at frequencies where wavevector matching is achieved, which, for a broadband light input, results in characteristic spectral dips in the light output. One of the advantages of the optical fibre configuration is that the incident light is always immersed in a dielectric, meaning that discrete coupling elements such as prisms are not required. However, both the polarization and incidence angle of light in the optical fibre core are not well defined, meaning that the efficiency of coupling is less than that achieved by the Kretschemann configuration.

4.3 Proposed Surface Plasmon Resonance Sensor

The proposed surface plasmon resonance sensor is depicted in Figure 4.5. Similar to other SPR device configurations, a thin metal film is used to en-

able light incident from an optically denser dielectric medium to couple to surface plasmons on the other side of the film. The film is deposited onto a clear polymer sheet, and the bottom of the polymer sheet is connected to a linear polarizing sheet using an optically transparent adhesive. A single-mode optical fibre is used to guide light towards to the metal film, and a multi-mode optical fibre is used to collect light reflected from the metal film. The light collected by the multi-mode fibre is analyzed by a spectrometer. A multi-mode fibre is used for light collection, as opposed to a single-mode fibre, due to its larger acceptance angle. The excitation and collection fibres are then connected to the bottom of the polarizer sheet using a drop of optical adhesive. The drop of optical adhesive connects the end of the excitation fibre to the bottom of the polarizer sheet, ensuring that light incident onto the metal film is always immersed in a dielectric. Complete immersion of the incident light in a dielectric precludes the requirement of a discrete coupling element, similar to optical-fibre-based SPR configurations.

Optical and geometrical parameters related to different layers of the SPR configuration is given in Table 4.1. Due to the similar refractive index values of the fibre, optical adhesive, polarizer sheet, and polymer sheet, little light is reflected from the dielectric interfaces of the sensor. One of the advantages of this configuration is that it integrates light delivery, polarization control, and surface plasmon coupling onto a single flexible substrate and enables interrogation of surface plasmon resonance by either angle tuning or wavelength tuning. An additional benefit is that the components are inexpensive and easily assembled, paving the way for disposable and commercially viable SPR sensors for single-use applications.

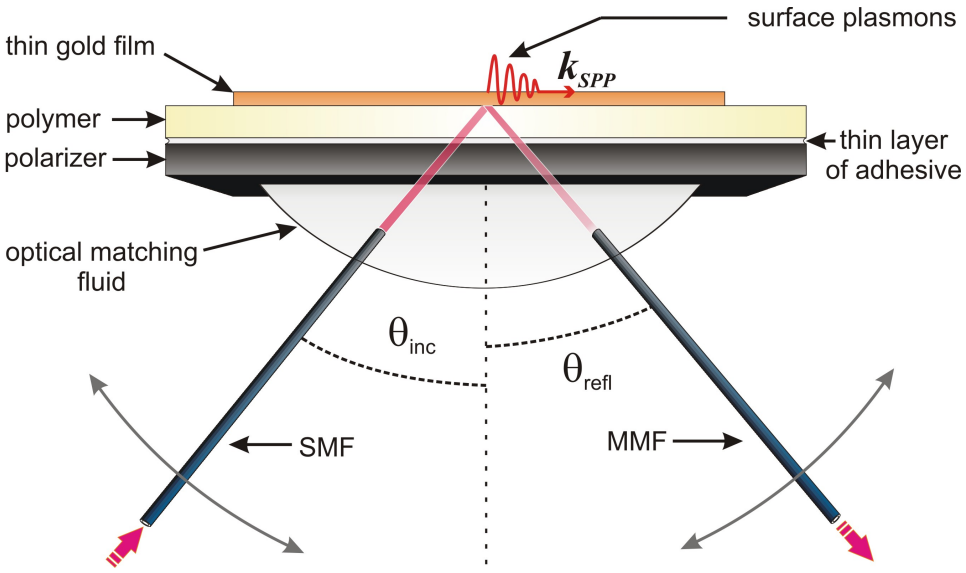

Figure 4.5: Proposed surface plasmon resonance sensor configuration. A thin metal film is deposited onto a clear plastic film. The bottom side of the plastic film is optically contacted with a linear polarizer sheet. Two optical fibres, one to input light and the other to collect the reflected light with full control over the incident and reflected angle, are then connected to the bottom of the linear polarizer sheet.

Table 4.1: Optical and geometrical parameters of the proposed surface plasmon resonance sensor

Layer material	Layer thickness	Material refractive index
Au	75 nm, 150 nm	Published data [62]
Polymer sheet	130 μm	1.5 - 1.6
Optical adhesive (thin)	30 μm	1.56
Polarizer sheet	110 μm	1.5
Optical adhesive (thick)	—	1.56
Optical fibre	—	1.49 - 1.5

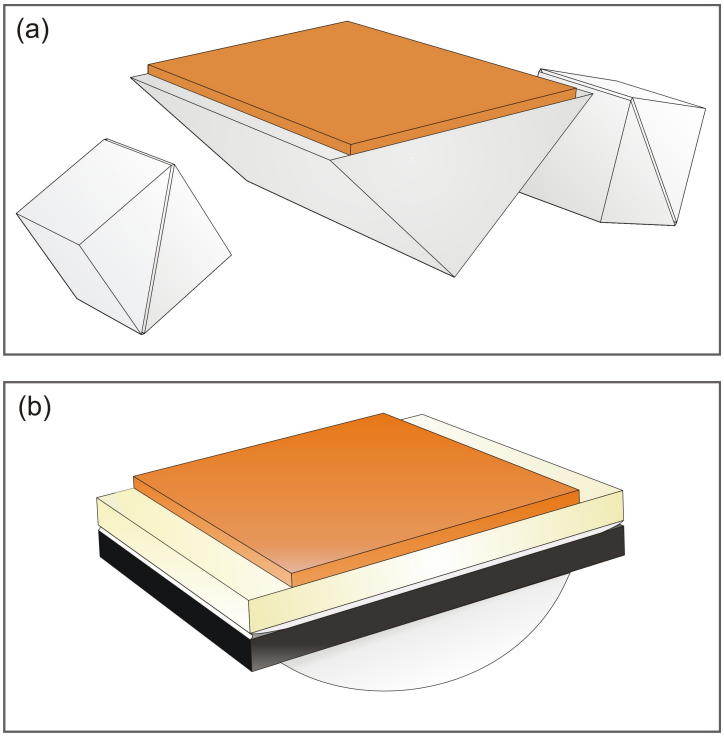

Figure 4.6: Schematic diagrams depicting (a) typical Kretchemann SPR configuration consisting of a thin metal film on a prism with two polarizing elements and (b) our integrated SPR configuration consisting of a thin metal film on a clear plastic sheet optically contacted to a polarizing sheet with a drop of optical adhesive below.

4.4 Measurement Methodology

Surface plasmon resonance is interrogated by measuring the reflectance of an Au film that has two regions of different thicknesses: a thin region that is 75- nm thick and a thick region that is 150- nm thick (Figure 4.7). The thicknesses of the two regions of the gold film are measured using a Dek Tak scanning profilometer. The thin region is optically semi-transparent and

permits light tunneling across the film, whereas the thick region is optically opaque and does not permit light tunneling across the film. Thus, light incident onto the thin portion of the film can couple to surface plasmons on the other side of the film, whereas light incident onto the thick portion of the film cannot couple to surface plasmons on the other side. We thus quantify a normalized reflectance by

$$R(\omega) = \frac{I_s(\omega) - I_d(\omega)}{I_c(\omega) - I_d(\omega)}, \tag{4.4}$$

where I_s is the intensity of light reflected from the thin region, I_c is the intensity of light reflected from the thick region, and I_d is the dark spectrum (corresponding to spectrometer noise recorded in the absence of light input).

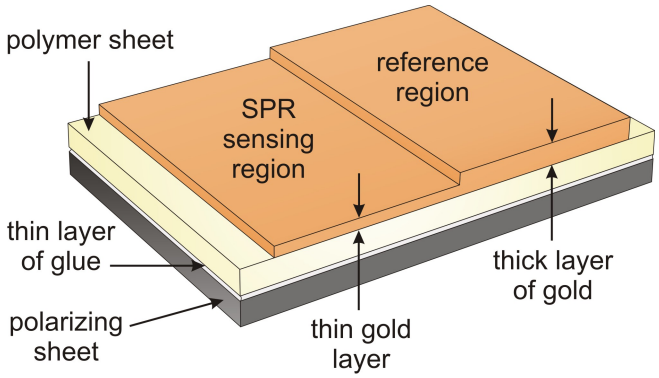

Figure 4.7: Schematic of the experimental surface plasmon resonance chip. The metallic layer on the clear plastic film consists of two regions: a thin region that is used for surface plasmon coupling and a thicker region that does not enable surface plasmon coupling. Reflection measurements from the thicker region are used to normalize reflection measurements from the thinner region.

The spectral intensities and resulting normalized reflectance are shown in Figure 4.8 for a representative case of $\theta = 45°$. The dip in the reflectance at $\lambda = 578\,\text{nm}$ is indicative of surface plasmon resonance.

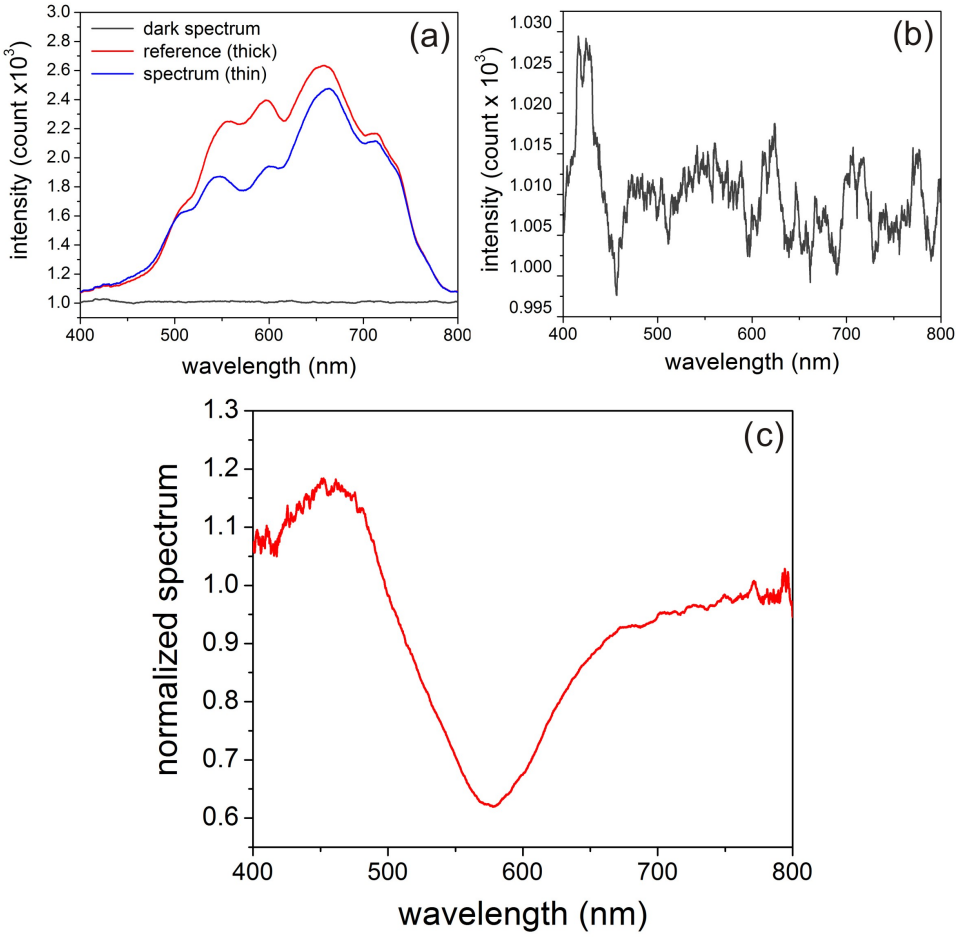

Figure 4.8: (a) Spectral reflection measurements from the 75- nm-thick (blue line) and the 150- nm-thick (red line) portions of an Au film for an angle of incidence of $\theta = 45°$. A dark measurement (black line) illustrates the baseline noise in the spectral measurements and is shown on a magnified scale in (b). (c) Normalized reflection measurement obtained from the spectral reflection measurements.

4.5 Multi-Layer Reflectivity Model

We model the reflectivity of a multi-layered system using transfer-matrix formalism [63–65]. Let's first consider a three layered system composed of regions m, n and k, as shown in Figure 4.9 (left). We label the regions 1 and 2 as the left and right sides of the interface m-n, respectively, and the regions 3 and 4 as the left and right sides of interface n-k, respectively.

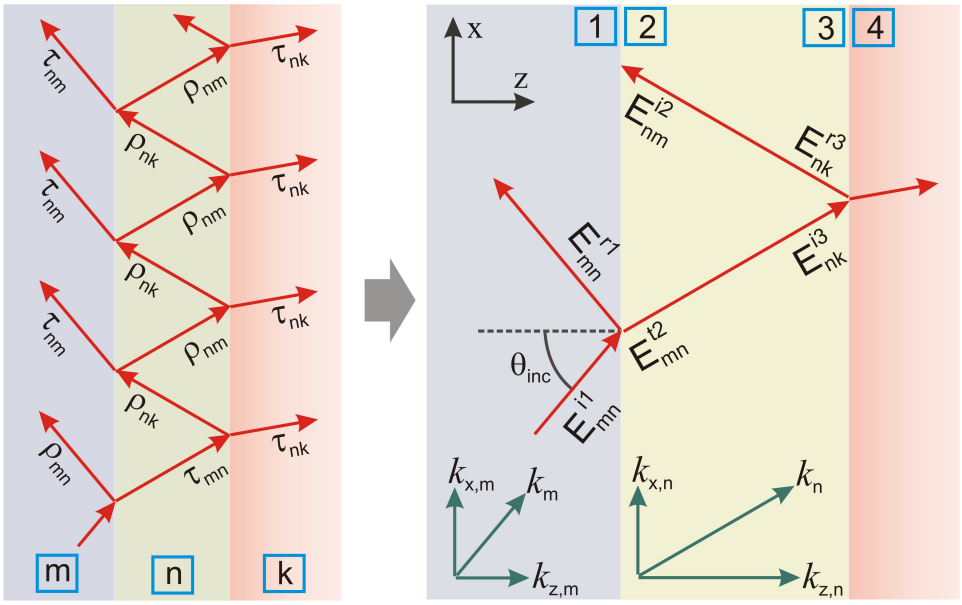

Figure 4.9: (left) Three-layer system representing a general multi-layered structure in terms of the reflection and transmission coefficients at each interface. (right) Model description in terms of the electric field, angle of incidence, and wavevector components.

As shown in Figure 4.9 (right), the electric field components and reflection and transmission coefficients are denoted by

E^{i1}_{mn} = Incident electric field from layer m to n at region 1,

E^{t2}_{mn} = Transmitted electric field from layer m to n at region 2,

E^{r3}_{nk} = Reflected electric field from layer n to k at region 3,

ρ_{mn} = Reflection coefficient for reflection from m-n interface to m,

τ_{mn} = Transmission coefficient for transmission from layer m to n.

For a transverse-magnetic polarized incident wave, the reflection and transmission coefficients [64] are given by

$$\rho_{mn} = \frac{1 - b_{mn}}{1 + b_{mn}}, \tag{4.5}$$

$$\tau_{mn} = \frac{2\left(\sqrt{\frac{\epsilon_m}{\epsilon_n}}\right)}{1 + b_{mn}}, \tag{4.6}$$

where ϵ_m and ϵ_n represent the complex permittivities of layer m and layer n, respectively, $k_{z,m}$ and $k_{z,n}$ are the normal components of the wavevector corresponding to layer m and n, respectively, and the parameter b_{mn} is given by

$$b_{mn} = \left(\frac{\epsilon_m}{\epsilon_n}\right)\left(\frac{k_{z,n}}{k_{z,m}}\right). \tag{4.7}$$

The transmission and reflection coefficients pertaining to a two-layer interface are related by

$$\rho_{mn} = -\rho_{nm}, \tag{4.8}$$

$$\rho^2_{mn} = 1 - \tau_{mn}\,\tau_{nm}. \tag{4.9}$$

The tangential component of the wavevector can be calculated at the interface using the boundary condition as

$$\begin{aligned} k_{x,m} &= k_{x,n}, \\ &= \left(\frac{2\pi}{\lambda}\right)\sqrt{\epsilon_m}\sin\,\theta_{\text{inc}} = k_0\sqrt{\epsilon_m}\sin\,\theta_{\text{inc}}, \end{aligned} \tag{4.10}$$

where λ is the free space wavelength of incident electric field. The normal components at each layer can be calculated using Snell's law as

$$k_{z,m} = \sqrt{{k_0}^2\,\epsilon_m - {k_{x,m}}^2}, \tag{4.11}$$

$$k_{x,n} = \sqrt{{k_0}^2\,\epsilon_n - {k_{x,n}}^2}. \tag{4.12}$$

Incorporating multiple reflections at layer n, as shown in Figure 4.6 (left), the incident field at region 1 can be related to the fields at region 2 by

$$\begin{aligned} E^{t2}_{mn} &= \tau_{mn}\,E^{i1}_{mn} + \rho_{mn}\,E^{i2}_{nm}\Big[1 + \Big(\rho_{nm}\rho_{nk}e^{-j\Delta\phi}\Big) \\ &\qquad + \Big(\rho_{nm}\rho_{nk}e^{-j\Delta\phi}\Big)^2 + \cdots\Big], \\ &= \tau_{mn}\,E^{i1}_{mn} + \frac{\rho_{nm}}{1 - \rho_{nm}\rho_{nk}e^{-j\Delta\phi}}\,E^{i2}_{nm}. \end{aligned} \tag{4.13}$$

Equation 4.13 can be rearranged as

$$\begin{aligned} E^{i1}_{mn} &= \frac{1}{\tau_{mn}}\,E^{t2}_{mn} - \frac{1}{\tau_{mn}}\left(\frac{\rho_{nm}}{1 - \rho_{nm}\rho_{nk}e^{-j\Delta\phi}}\right)E^{i2}_{nm}, \\ &= \frac{1}{\tau_{mn}}\left[E^{t2}_{mn} + \left(\frac{\rho_{mn}}{1 + \rho_{mn}\rho_{nk}e^{-j\Delta\phi}}\right)E^{i2}_{nm}\right], \end{aligned} \tag{4.14}$$

where $\Delta\phi = 2\,\beta_n$ and $\beta_n = k_{z,n}d_n$ are the parameters associated with propagation over $2d_n$ and d_n, respectively. E^{r1}_{mn}, which consists of contributions from the reflected and transmitted field at region 1, can also be expressed as a function of fields at region 2

$$\begin{aligned} E^{r1}_{mn} &= \rho_{mn}\,E^{i1}_{mn} + \tau_{nm}\,E^{i2}_{nm}\Big[1 + \Big(\rho_{nm}\rho_{nk}e^{-j\Delta\phi}\Big) \\ &\qquad + \Big(\rho_{nm}\rho_{nk}e^{-j\Delta\phi}\Big)^2 + \cdots\Big]. \end{aligned} \tag{4.15}$$

Replacing Eqn. 4.14 into Eqn. 4.15 and simplifying the series, we get

$$\begin{aligned} E^{r1}_{mn} &= \rho_{mn}\left[\frac{1}{\tau_{mn}}\,E^{t2}_{mn} - \frac{1}{\tau_{mn}}\left(\frac{\rho_{nm}}{1-\ \rho_{nm}\rho_{nk}e^{-j\Delta\phi}}\right)E^{i2}_{nm}\right] \\ &\quad + \frac{\tau_{nm}}{1-\ \rho_{nm}\rho_{nk}e^{-j\Delta\phi}}\,E^{i2}_{nm}. \end{aligned} \tag{4.16}$$

Rearranging Eqn. 4.16

$$\begin{aligned} E^{r1}_{mn} &= \frac{\rho_{mn}}{\tau_{mn}}\,E^{t2}_{mn} + \frac{-\,\rho_{nm}\,\rho_{mn} + \,\tau_{mn}\,\tau_{nm}}{\tau_{mn}(1-\ \rho_{nm}\rho_{nk}e^{-j\Delta\phi})}\,E^{i2}_{nm}, \\ &= \frac{\rho_{mn}}{\tau_{mn}}\,E^{t2}_{mn} + \frac{(\,\rho_{mn})^2 + \,\tau_{mn}\,\tau_{nm}}{\tau_{mn}(1+\ \rho_{mn}\rho_{nk}e^{-j\Delta\phi})}\,E^{i2}_{nm}. \end{aligned} \tag{4.17}$$

Equation 4.17 can be re-arranged into the form

$$\begin{aligned} E^{r1}_{mn} &= \frac{\rho_{mn}}{\tau_{mn}}\,E^{t2}_{mn} + \frac{1}{\tau_{mn}(1+\ \rho_{mn}\rho_{nk}e^{-j\Delta\phi})}\,E^{i2}_{nm}, \\ &= \frac{1}{\tau_{mn}}\left[\rho_{mn}\,E^{t2}_{mn} + \frac{1}{1+\ \rho_{mn}\rho_{nk}e^{-j\Delta\phi}}\,E^{i2}_{nm}\right]. \end{aligned} \tag{4.18}$$

Comparing Eqns. 4.14 and 4.18, a matrix equation can be derived

$$\begin{aligned} \begin{bmatrix} E^{i1}_{mn} \\ E^{r1}_{mn} \end{bmatrix} &= \frac{1}{\tau_{mn}}\begin{bmatrix} 1 & \frac{\rho_{mn}}{1+\,\rho_{mn}\rho_{nk}e^{-j\Delta\phi}} \\ \rho_{mn} & \frac{1}{1+\,\rho_{mn}\rho_{nk}e^{-j\Delta\phi}} \end{bmatrix}\begin{bmatrix} E^{t2}_{mn} \\ E^{i2}_{nm} \end{bmatrix}, \\ &= \frac{1}{\tau_{mn}}\begin{bmatrix} 1 & M\,\rho_{mn} \\ \rho_{mn} & M \end{bmatrix}\begin{bmatrix} E^{t2}_{mn} \\ E^{i2}_{nm} \end{bmatrix}, \end{aligned} \tag{4.19}$$

where

$$M = \frac{1}{1+\ \rho_{mn}\rho_{nk}e^{-j\Delta\phi}}. \tag{4.20}$$

Equation 4.19 relates the electric fields at region 1 and 2. Fields at region 2

and region 3 can be related using the relationship

$$E_{nk}^{i3} = E_{mn}^{t2} e^{-j\,k_{z,n} d_n}, \tag{4.21}$$

$$E_{nk}^{r3} = E_{nm}^{i2} e^{j\,k_{z,n} d_n}, \tag{4.22}$$

which can be rearranged as

$$E_{mn}^{t2} = E_{nk}^{i3} e^{j\,k_{z,n} d_n}, \tag{4.23}$$

$$E_{nm}^{i2} = E_{nk}^{r3} e^{-j\,k_{z,n} d_n}. \tag{4.24}$$

Writing the above equations in matrix form yields

$$\begin{bmatrix} E_{mn}^{t2} \\ E_{nm}^{i2} \end{bmatrix} = \begin{bmatrix} e^{j\,\beta_n} & 0 \\ 0 & e^{-j\,\beta_n} \end{bmatrix} \begin{bmatrix} E_{nk}^{i3} \\ E_{nk}^{r3} \end{bmatrix}. \tag{4.25}$$

Combining Eqns. 4.19 and 4.25, we get

$$\begin{bmatrix} E_{mn}^{i1} \\ E_{mn}^{r1} \end{bmatrix} = \frac{1}{\tau_{mn}} \begin{bmatrix} 1 & M\,\rho_{mn} \\ \rho_{mn} & M \end{bmatrix} \begin{bmatrix} e^{j\,\beta_n} & 0 \\ 0 & e^{-j\,\beta_n} \end{bmatrix} \begin{bmatrix} E_{nk}^{i3} \\ E_{nk}^{r3} \end{bmatrix}. \tag{4.26}$$

Fields at region 1 and 3 can now be related by a transmission matrix,

$$\mathbf{T} = \frac{1}{\tau_{mn}} \begin{bmatrix} 1 & M\,\rho_{mn} \\ \rho_{mn} & M \end{bmatrix}, \tag{4.27}$$

and a propagation matrix,

$$\mathbf{P} = \begin{bmatrix} e^{j\,\beta_n} & 0 \\ 0 & e^{-j\,\beta_n} \end{bmatrix}. \tag{4.28}$$

The system matrix, $\mathbf{S}$, for a three-layer unit can be achieved by cascading $\mathbf{T}$ and $\mathbf{P}$, written as

$$\mathbf{S} = \mathbf{T} * \mathbf{P} = \begin{bmatrix} S_{11} & S_{12} \\ S_{21} & S_{22} \end{bmatrix}. \tag{4.29}$$

Reflectance of the three layer stack can now be calculated as a ratio of E_{mn}^{r1} and E_{mn}^{i1}, which are related through the elements in the system matrix. To model the reflectance of the multilayered SPR sensor, which consists of a thick layer of optical adhesive, a polarizer sheet, a thin layer of optical adhesive, a polymer substrate, an Au layer, and the superstrate region (which in this case is air), we derive the system matrix for a six-layered system given by

$$\begin{aligned} \mathbf{S} &= \mathbf{T}_1 * \mathbf{P}_1 * \mathbf{T}_2 * \mathbf{P}_2 * \mathbf{T}_3 * \mathbf{P}_3 * \mathbf{T}_4 * \mathbf{P}_4 * \mathbf{T}_5, \\ &= \begin{bmatrix} S_{11} & S_{12} \\ S_{21} & S_{22} \end{bmatrix}, \end{aligned} \tag{4.30}$$

where $\mathbf{T}_1$ and $\mathbf{P}_1$ correspond to the polarizer sheet, $\mathbf{T}_2$ and $\mathbf{P}_2$ correspond to the thin optical adhesive layer, $\mathbf{T}_3$ and $\mathbf{P}_3$ correspond to the polymer substrate, $\mathbf{T}_4$ and $\mathbf{P}_4$ correspond to the Au layer, and $\mathbf{T}_5$ corresponds to the superstrate region. The reflectance of the six-layered system can be calculated from the system matrix as

$$R = \left| \frac{S_{21}}{S_{11}} \right|^2. \tag{4.31}$$

Normalized reflectance is obtained by calculating reflectance values for the thin Au layer and normalizing by reflectance values for the thick Au layer.

4.6 Results and Discussion

We first measure the normalized reflectance of the SPR sensor for an incident wave that is transverse electric polarized. Figure 4.10(a) plots the normalized reflectance spectra for incidence angles from 41° to 49°, where, notably, no resonance dip is measured. The measurements are corroborated by the model calculations, performed for the case of index mismatch [Table 4.1] between the dielectric layers [Figure 4.10(b)] and the case of perfect index matching between the dielectric layers [Figure 4.10(c)]. Both the experiment and model calculations suggest the absence of surface plasmon resonance for transverse electric incidence polarization.

We next measure the normalized reflectance for an incident wave that is transverse magnetic polarized. Figure 4.11(a) plots the normalized reflectance spectra for incidence angles from 42° to 47°. A pronounced dip is observed in the normalized reflectance spectra for all incidence angles. As the incidence angle increases, the position of the dip shifts towards smaller wavelengths which is in good agreement with the dispersion curve of surface plasmon. As seen in Figures 4.11(b) and (c), the model also predicts dips in the normalized reflectance, which have a similar magnitude to those observed in the experiment. Model predictions of the spectral position of the dip as a function of incidence angle agree well with experimental measurements, as highlighted in Table 4.2. The approximately 1° offset between the model calculations and experiment may arise from a small tilt in the sensor position.

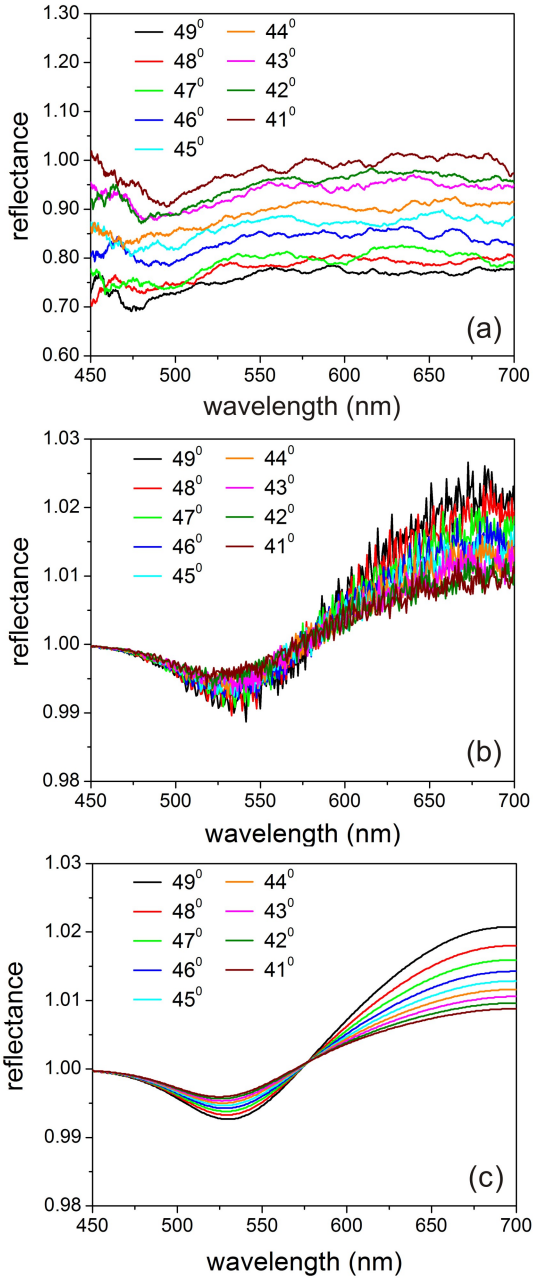

Figure 4.10: (a) Normalized reflectance measurement for various angles of incidence for transverse-electric incident polarization. Model predictions of the normalized reflectance for the case of (b) imperfect index matching and (c) perfect index matching between the multiple substrate layers.

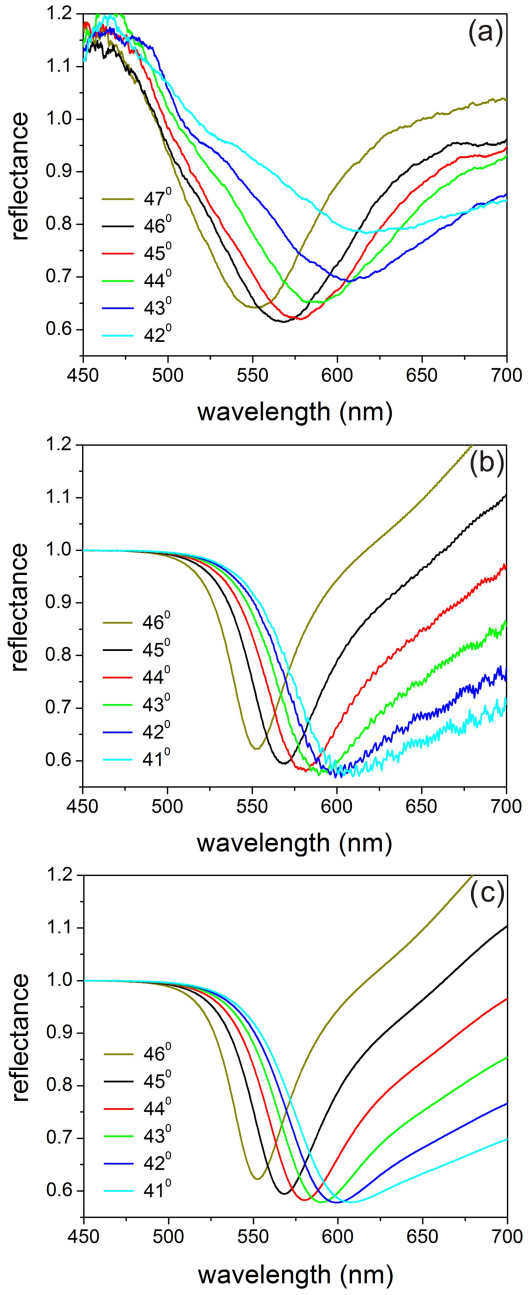

Figure 4.11: (a) Normalized reflectance measurement for various angles of incidence for transverse-magnetic incident polarization. Model predictions of the normalized reflectance for the case of (b) imperfect index matching and (c) perfect index matching between the multiple substrate layers.

Table 4.2: Resonance wavelength (λ_{res}) and corresponding incident angle

Experiment		Model	
θ_{inc} (degree)	λ_{res} (nm)	θ_{inc} (degree)	λ_{res} (nm)
47	551.322	46	551.97
46	568.29	45	568.11
45	578.11	44	579.34
44	589.05	43	589.16
43	606.72	42	602.49
42	616.75	41	613.01

4.7 Summary

We have presented a new SPR device architecture that exploits the wide availability of guided optics and index-matched fluids. The device consists of a thin metal film on a polymer sheet, which is connected to a linear polarizer sheet. Optical fibres are used to guide light to and from the metal film. The resulting SPR device has the advantages of low cost, compactness, and amenability for single-use applications. We have characterized the device for both transverse-magnetic and transverse-electric polarization and have found good agreement with a transfer-matrix model.

Chapter 5

Conclusions

Optical components constructed from fluids have several advantages over those constructed from solid materials, including increased tunability, lower cost of fabrication, and naturally smooth surfaces. In this thesis, we have explored two optical systems in which small volumes of fluids have been used to manipulate and control the flow of light, and have highlighted both the advantages and disadvantages of this approach.

In one application, we have constructed a fluidic lens based on a water droplet attached to the end of a syringe. The droplet shape can be tuned by both applying an external pressure and manipulating the droplet volume through the injection or withdrawal of fluid to achieve variable focus and magnification. We have characterized the focussing properties of the droplet lens as a function of the droplet size and used the droplet as the objective lens in both reflection-mode and transmission-mode microscope configurations. The images captured by the droplet microscope show micron-scale resolution and quality comparable to that obtained by a conventional laboratory-grade microscope. As opposed to other liquid lens implementation methods that require elaborate housing structures and multiple micro- or nano-fabrication steps, the droplet lens developed in Chapter 3 exploits low-cost and widely-

available techniques to dispense and shape small volumes of fluids. A fluidic coating technique has been discovered which yields a highly stable water droplet structure in ambient air that is addressable by free-space illumination. A key feature of the droplet lens is that the lens can be created on demand and can be discarded after use with little waste of materials. The low cost of implementation, wide accessibility of the requisite materials, relative simplicity of operation, and good quality of images obtained suggests that microscopy using water droplets may be viable for resource-limited regions.

In the second application, we have constructed a new surface plasmon resonance (SPR) sensor based on fibre optics and index-matched fluids. Conventional SPR sensors require discrete optical coupling elements, such as a prism and a polarizer, to enable free-space light to couple to surface plasmons on a metal film. We have circumvented this requirement by designing a SPR sensor in which light delivered to the surface plasmon substrate is always immersed in a dielectric. This was achieved by optically attaching input and output optical fibres, a polarizer, and a surface plasmon substrate using index matching fluid. The fluid physically binds the different components of the sensor and provides an unimpeded pathway for light incident onto the metal film. We have demonstrated the working principle of the SPR sensor, experimentally characterized the performance of a prototype device, and compared our experimental findings with theoretical predictions based on a reflectivity model. The new SPR sensor configuration is more compact and cost-effective than the conventional prism configuration. An additional benefit is that the components used are inexpensive and easily

assembled, which paves the way for disposable and commercially-viable SPR sensors that can be used for single-use applications.

Bibliography

[1] P. Mach, M. Dolinski. K. W. Baldwin, J. A. Rogers, C. Kerbage, R. S. Windeler and B. J. Eggleton, "Tunable microfluidic optical fiber," *Appl. Phys. Lett.*, vol. 80, no. 23, pp. 4294–4296, 2002.

[2] F. Cattaneo, K. Baldwin, Shu Yang, T. Krupenkine, S. Ramachandran and J.A. Rogers, "Digitally tunable microfluidic optical fiber devices," *Appl. Phys. Lett.*, vol. 12, no. 6, pp. 907–912, 2003.

[3] J. P. Dowling, M. Scalora, M. J. Bloemer, and C. M. Bowden, "The photonic band edge laser: A new approach to gain enhancement," *J. Appl. Phys.*, vol. 75, no. 4, pp. 1896–1899, 1994.

[4] K. W. Ro, K. Lim, B. C. Shim, C. Bong and J. H. Hahn, "Integrated light collimating system for extended optical-path-length absorbance detection in microchip-based capillary electrophoresis," *Anal. Chem.*, vol. 77, no. 16, pp. 5160–5166, 2005.

[5] D. Psaltis, S. R. Quake and C. Yang, "Developing optofluidic technology through the fusion of microfluidics and optics," *Nature*, vol. 442, no. 7101, pp. 381 – 386, 2006.

[6] C. Monat, P. Domachuk and B. J. Eggleton, "Integrated optofluidics: A new river of light," *Nat. Photon*, vol. 1, no. 2, pp. 106–114, 2007.

[7] D. Erickson, D. Sinton and D. Psaltis, "Optofluidics for energy applications," *Nat. Photon*, vol. 5, no. 10, pp. 583–590, 2011.

[8] "Optofluidics: field or technique?" *Lab Chip*, vol. 8, pp. 1856–1863, 2008.

[9] Y. Hongbin, Z. Guangya, C. F. Siong and W. Shouhua, "Lens with transformable-type and tunable-focal-length characteristics," *IEEE J. Sel. Top. Quant.*, vol. 15, no. 5, pp. 1317 – 1322, 2009.

[10] L. Dong, A.K Agarwal, D. J. Beebe and H. Jiang, "Adaptive liquid microlenses activated by stimuli-responsive hydrogels," *Nature*, vol. 442, no. 7102, pp. 551–554, 2006.

[11] S. Xu, H. Ren, Y.-J. Lin, M. G. J. Moharam, S.-T. Wu, and N. Tabiryan, "Adaptive liquid lens actuated by photo-polymer," *Opt. Express*, vol. 17, no. 20, pp. 17 590–17 595, 2009.

[12] H. B. Yu, G. Y. Zhou, F. S. Chau, F. W. Lee, S. H. Wang, and H. M. Leung, "A liquid-filled tunable double-focus microlens," *Opt. Express*, vol. 17, no. 6, pp. 4782–4790, 2009.

[13] H.-M. Son, M. Y. Kim, and Y.-J. Lee, "Tunable-focus liquid lens system controlled by antagonistic winding-type sma actuator," *Opt. Express*, vol. 17, no. 16, pp. 14 339–14 350, 2009.

[14] Agilent, "Introducing the agilent photomic switching platform," 2000. [Online]. Available: http://web.pdx.edu/~larosaa/Agilent_All_Optical_Network.htm

[15] Sindy K. Y. Tang, Claudiu A. Stan and George M. Whitesides, "Dynamically reconfigurable liquid-core liquid-cladding lens in a microfluidic channel," *Lab Chip*, vol. 8, pp. 395–401, 2008.

[16] S.-K. Hsiung, C.-H. Lee, and G.-B. Lee, "Microcapillary electrophoresis chips utilizing controllable micro-lens structures and buried optical fibers for on-line optical detection." *Electrophoresis*, vol. 29, no. 9, pp. 1866–1873, 2008.

[17] M. Bass, C. DeCusatis, J. Enoch, V. Lakshminarayanan, G. Li, C. MacDonald, V. Mahajan and E. V. Stryland, *Handbook of Optics, Third Edition, Volume I: Geometrical and Physical Optics, Polarized Light, Components and Instruments(set), Sponsored by Optical Society of America.* McGraw-Hill, 2010.

[18] D. B. Murphy, *Fundamentals of Light Microscopy and Electronic Imaging.* Wiley-Liss, 2001.

[19] M. Expressions, "Molecular expressions - optical microscopy primer," 2012. [Online]. Available: http://micro.magnet.fsu.edu/primer/index.html

[20] Olympus, "Olympus - microscopy resource center," 2012. [Online]. Available: http://www.olympusmicro.com/index.html

[21] Zeiss, "Zeiss campus - education of microscopy and digital imaging," 2012. [Online]. Available: http://zeiss-campus.magnet.fsu.edu/index.html

[22] The images have been adapted from [19–21].

[23] A. H. Bennett, "The development of the microscope objective," *J. Opt. Soc. Am.*, vol. 33, no. 3, pp. 123–123, 1943.

[24] D. W. Piston, "Choosing objective lenses: The importance of numerical aperture and magnification in digital optical microscopy," *Biol. Bull.*, vol. 195, no. 195, pp. 1–4, 1998.

[25] P. Evennett and C. Hammond, "Microscopy — overview," in *Encyclopedia of Analytical Science*, second edition ed. Oxford: Elsevier, 2005, pp. 32 – 41.

[26] M. W. Davidson and M. Abramowitz, "Optical microscopy," *Encycl. of Imag. Sci. and Tech.*, vol. 2, no. 2, pp. 1106–1140, 2002.

[27] E. Hecht and A. Zajac, *Optics*. Addison-Wesley, New York, 1975.

[28] M. Abramowitz, K. R. Spring, H. E. Keller and M. W. Davidson, "Basic principles of microscope objectives," *BioTechniques*, vol. 33, no. 33, pp. 772–781, 2002.

[29] D. Psaltis, S. R. Quake and C. Yang, "Developing optofluidic technology through the fusion of microfluidics and optics," *Nature (London)*, vol. 442, pp. 381–386, 2006.

[30] L. Commander, S. Day, and D. Selviah, "Variable focal length microlenses," *Opt. Commun.*, vol. 177, no. 1-6, pp. 157 – 170, 2000.

[31] B. Berge and J. Peseux, "Variable focal lens controlled by an external voltage: An application of electrowetting," *Eur. Phys. J. E*, vol. 3, no. 2, pp. 159–163, 2000.

[32] H. H. Myint, A. M. Marpaung, H. Kurniawan, H. Hattori and K. Kagawa, "Water droplet lens microscope and microphotographs," *Phys. Education*, vol. 36, pp. 97–101, 2001.

[33] T. Krupenkin, S. Yang, and P. Mach, "Tunable liquid microlens," *Appl. Phys. Lett.*, vol. 82, no. 3, pp. 316–318, 2003.

[34] C.-C. Cheng, C. A. Chang, and J. A. Yeh, "Variable focus dielectric liquid droplet lens," *Opt. Express*, vol. 14, no. 9, pp. 4101–4106, 2006.

[35] H. Ren, H. Xianyu, S. Xu, and S.-T. Wu, "Adaptive dielectric liquid lens," *Opt. Express*, vol. 16, no. 19, pp. 14 954–14 960, 2008.

[36] S. Kuiper and B. H. W. Hendriks, "Variable-focus liquid lens for miniature cameras," *Appl. Phys. Lett.*, vol. 85, no. 7, pp. 1128–1130, 2004.

[37] Varioptic, "Varioptic - the liquid lens company," 2011. [Online]. Available: http://www.varioptic.com/en/products.html

[38] S. Xu, H. Ren, Y. Liu, and S.-T. Wu, "Dielectric liquid microlens with switchable negative and positive optical power," *J. Microelectromech. S.*, vol. 20, no. 1, pp. 297 –301, 2011.

[39] H. Ren and S.-T. Wu, "Variable-focus liquid lens by changing aperture," *Appl. Phys. Lett.*, vol. 86, no. 21, p. 211107, 2005.

[40] F. S. Tsai, S. H. Cho, Y.-H. Lo, B. Vasko, and J. Vasko, "Miniaturized universal imaging device using fluidic lens," *Opt. Lett.*, vol. 33, no. 3, pp. 291–293, 2008.

[41] H. Oku, K. Hashimoto, and M. Ishikawa, "Variable-focus lens with 1-khz bandwidth," *Opt. Express*, vol. 12, no. 10, pp. 2138–2149, 2004.

[42] H. Ren and S.-T. Wu, "Variable-focus liquid lens," *Opt. Express*, vol. 15, no. 10, pp. 5931–5936, 2007.

[43] G.-H. Feng and Y.-C. Chou, "Flexible meniscus/biconvex lens system with fluidic-controlled tunable-focus applications," *Appl. Optics*, vol. 48, no. 18, pp. 3284–3290, 2009.

[44] N. Chronis, G. Liu, K.-H. Jeong, and L. Lee, "Tunable liquid-filled microlens array integrated with microfluidic network," *Opt. Express*, vol. 11, no. 19, pp. 2370–2378, 2003.

[45] K.-H. Jeong, G. Liu, N. Chronis, and L. Lee, "Tunable microdoublet lens array," *Opt. Express*, vol. 12, no. 11, pp. 2494–2500, 2004.

[46] D.-Y. Zhang, V. Lien, Y. Berdichevsky, J. Choi, and Y.-H. Lo, "Fluidic adaptive lens with high focal length tunability," *Appl. Phys. Lett.*, vol. 82, no. 19, pp. 3171–3172, 2003.

[47] P. M. Moran, S. Dharmatilleke, A. H. Khaw, K. W. Tan, M. L. Chan,

and I. Rodriguez, "Fluidic lenses with variable focal length," *Appl. Phys. Lett.*, vol. 88, no. 4, p. 041120, 2006.

[48] X. Mao, J. R. Waldeisen, B. K. Juluri, and T. J. Huang, "Hydrodynamically tunable optofluidic cylindrical microlens," *Lab Chip*, vol. 7, pp. 1303–1308, 2007.

[49] H. Ren, D. Fox, P. A. Anderson, B. Wu, and S.-T. Wu, "Tunable-focus liquid lens controlled using a servo motor," *Opt. Express*, vol. 14, no. 18, pp. 8031–8036, 2006.

[50] H.-M. Son, M. Y. Kim, and Y.-J. Lee, "Tunable-focus liquid lens system controlled by antagonistic winding-type sma actuator," *Opt. Express*, vol. 17, no. 16, pp. 14 339–14 350, 2009.

[51] S. Reichelt and H. Zappe, "Design of spherically corrected, achromatic variable-focus liquid lenses," *Opt. Express*, vol. 15, no. 21, pp. 14 146–14 154, 2007.

[52] M. L. Brongersma and P. G. Kik, *Surface plasmon nanophotonics*. Springer, 2007.

[53] S. A. Maier, *Plasmonics: Fundamentals and Applications*. Springer, 2007.

[54] K. Park, B. J. Lee, C. Fu, and Z. M. Zhang, "Study of the surface and bulk polaritons with a negative index metamaterial," *J. Opt. Soc. Am. B*, vol. 22, no. 5, pp. 1016–1023, 2005.

[55] J. Homola, *Surface Plasmon Resonance Based Sensors*. Springer Series on Chemical Sensors and Biosensors: Methods and Applications, 2006.

[56] N. J. de Mol and M. J. E. Fischer, *Surface Plasmon Resonance: Methods and Protocols*. Springer Protocols, Methods in Molecular Biology 627, Humana Press, 2010.

[57] A. Otto, "Excitation of nonradiative surface plasma waves in silver by the method of frustrated total reflection," *Z. Phys. A-Hadron. Nucl.*, vol. 216, pp. 398–410, 1968.

[58] E. Kretschmann and H. Raether, "Radiative decay of non-radiative surface plasmons excited by light," *Z. Naturforsch. A*, vol. 23, no. 12, p. 2135, 1968.

[59] E. Kretschmann, "Decay of non radiative surface plasmons into light on rough silver films. comparison of experimental and theoretical results," *Opt. Commun.*, vol. 6, no. 2, pp. 185 – 187, 1972.

[60] R. Jorgenson and S. Yee, "A fiber-optic chemical sensor based on surface plasmon resonance," *Sensor Actuat. B: Chem*, vol. 12, no. 3, pp. 213 – 220, 1993.

[61] J. Homola, "Optical fiber sensor based on surface plasmon excitation," *Sensor Actuat. B: Chem*, vol. 29, no. 1-3, pp. 401 – 405, 1995, proceedings of the 2nd European Conference on Optical Chemical Sensors and Biosensors.

[62] P. B. Johnson and R. W. Christy, "Optical constants of the noble metals," *Phys. Rev. B*, vol. 6, pp. 4370–4379, 1972.

[63] B. Gupta and A. K. Sharma, "Sensitivity evaluation of a multilayered surface plasmon resonance-based fiber optic sensor: a theoretical study," *Sensor Actuat. B: Chem*, vol. 107, no. 1, pp. 40 – 46, 2005, proceedings of the 7th European Conference on Optical Chemical Sensors and Biosensors.

[64] K. Klein and T. E. Furtak, *Optics*. 2nd Edition, Wiley, New York, 1986.

[65] M. Kanso, S. Cuenot, and G. Louarn, "Sensitivity of optical fiber sensor based on surface plasmon resonance: Modeling and experiments," *Plasmonics*, vol. 3, pp. 49–57, 2008.